A Numerical Study of the Dynamics of Detonation Initiated by Cavity Collapse

A. K. Kapila, D. W. Schwendeman, J. Gambino and W. D. Henshaw
Department of Mathematical Sciences, Rensselaer Polytechnic Institute,
Troy, New York, 12180

August 7, 2014

Abstract

The dynamics of detonation evolution in a condensed-phase explosive, initiated by the shock-induced collapse of an embedded, ellipsoidal, gas-filled cavity, is examined computationally. Attention is focused on the details of the evolutionary process following the collapse. The reaction rate is assumed to be pressure-dependent, switching on when the pressure exceeds an ignition threshold. The strength of the incident shock is taken to be such that the reaction would not be initiated without the interaction of the shock with the cavity. The system is modeled as a multi-material mixture, and a high-resolution, Godunov type capturing scheme is employed to solve the governing equations numerically. The computations are carried out in parallel, and adaptive mesh refinement is used to obtain accurate and well-resolved solutions. It is found that collapse of the cavity produces a detonation provided the cavity is large enough, or the rate of reaction strong enough; otherwise reaction initiated by the collapse fizzles out. Details of how the detonation is is established are found to depend strongly upon the shape of the cavity.

1 Introduction

It is well known that the stimulus required to initiate a detonation in a heterogeneous, condensed-phase explosive is weaker than that needed to produce a similar event in a homogeneous explosive. When the initiating agent is a shock, the interaction of the shock with the microstructure of the medium leads to the generation of a nonuniform post-shock field that includes *hot spots* where local pressures and temperatures are higher than those that the incident shock would produce in a homogeneous environment. Chemical reaction originates preferentially at these sites before spreading to the bulk. Heterogeneities occur naturally in a granular explosive where the grains of the reactant are held together by a plastic binder. Additional contributors to heterogeneity include impurities, voids, inclusions and gas-filled cavities. Often cavities in the form of glass micro-balloons are introduced into liquid explosives by design to increase their sensitivity. A variety of mechanisms acting at the scale of the heterogeneities have been proposed for the creation of hot spots, including friction, cracking, dislocation pileup, local plastic deformation, and adiabatic heating of trapped gases. However, it is the collapse of gas-filled cavities and the high pressures and temperatures resulting therefrom that is recognized to be a dominant mechanism.

The degree to which the presence of cavities renders the explosive more susceptible to detonation is determined collectively by their number, size, shape and distribution. In this study we focus on a *single* cavity embedded in an otherwise homogeneous explosive, and explore the extent to which its collapse enhances the proclivity of the explosive towards detonation. It is assumed that the incident shock is planar, that the reaction rate is pressure-dependent, and that the reaction is switched on when pressure in the explosive medium rises above an ignition threshold. The strength of the incident shock is taken to be such that the post-shock pressure, without the aid of cavity collapse, is below the ignition threshold. We consider a spherical cavity and examine the post-collapse behavior as a function of the cavity size, to determine how large the cavity needs to be to ensure an established detonation as the outcome. The role played by the shape of the cavity is also assessed by repeating the computations for cavities shaped as prolate

and oblate spheroids. The post-collapse evolution is mapped out in detail, with emphasis on the fields of pressure and reaction progress. Attention is focused on identifying regions of the flow in which shock-cavity interaction results in pressures that are high enough to initiate reaction. The intent is to determine how the reaction intensifies and couples with the collapse-induced high pressure in the solid explosive to create a detonation, or fails to do so, and how this process depends upon the shape and size of the cavity and the strength of the reaction rate. This work is a natural extension of our earlier investigation [1] of single cavity collapse in an inert medium. The aim of that work was to obtain an accurate numerical description of the deforming interface and the ensuing flow structures, and to gain an understanding of the underlying physical mechanisms.

Cavity collapse and energy localization in the context of explosive ignition has been the subject of many previous investigations, both experimental and theoretical. (Existing literature on cavity collapse in areas of engineering application other than explosive ignition was described in detail in [1] and will not be repeated here.) The experimental work is well-summarized in the review by Bourne [2]. Also noteworthy are the experiments on cavity collapse in porous explosives by Bourne and Field [3]. These experiments are two-dimensional, with the cavity being a circular disk punched in a planar sheet of gelatinous material or in a sheet of emulsion explosive, and subject to a planar shock. Multiple cavities arranged in an array are also considered. The primary conclusion is that the incident shock induces convergent flow at the back of the cavity wall and forms a high-speed jet. The site of maximum temperature is behind the point of impact of the jet with the cavity wall. The authors note that other locations of elevated temperature may also arise as a result of complex hydrodynamic interactions generated by the incident shock, and that the size of the cavity plays an important role in determining the location of the ignition sites. In recent work, Swantek and Austin [4] have studied the collapse of a single void, as well as that of inline and offset arrays of multiple voids, under a stress-wave loading, again in a gelatinous medium and in a two-dimensional setting. It is found that the diffraction of the incident stress wave around the lead void, and the generation of a pulse of high pressure due to the collapse of the lead void, may cause the lead void to act either as a collapse inhibitor or a collapse trigger for the voids downstream, depending upon the array configuration and the void spacing.

Computational studies of cavity collapse motivated by hot-spot formation include the work of Milne and Bourne [5] aimed at simulating the experiments of Bourne and Field [3] noted above. Figures demonstrating the final stages of the collapse of the cavity are presented and show the formation of lobes subsequent to the jet impact. It is mentioned that temperatures attained during collapse are a strong function of the assumptions about the equations of state. Tran and Udaykumar [6, 7] have examined the collapse of a void in both an inert medium and a reactive medium, demonstrating the different ways in which energy localization can occur, ranging from plastic deformation to hydrodynamic collapse. This work is extended for the inert case to an array of voids by Kapahi and Udaykumar [8]. They also find that void-void interaction can either enhance or diminish the maximum post-shock pressure depending upon the location of the downstream voids. Lauer et al. [9] have examined the collapse of a cavity array, with particular emphasis on the maximum pressure attained. They observe that a smaller void-to-void distance generally, but not necessarily, results in large collapse pressure, and stress that exceptions from the general trend are due to complex hydrodynamic interactions. Michael and Nikiforakis [10] simulate the collapse of a single cavity in liquid nitromethane and in a two-dimensional configuration, and find that temperature maxima subsequent to collapse occur at locations directly in front of and behind the collapsed cavity.

What distinguishes this study from previous investigations is its focus on the full details of the hydrodynamic evolution that begins with the initiation of cavity collapse and culminates in either the establishment of a fully-developed detonation wave or in reaction extinction following partial reactant consumption. The way in which the evolutionary details depend upon the size and shape of the cavity and the reaction rate are also emphasized.

The situation under study in this work is an example of a multi-material system in which the principal constituents, the solid outside the cavity and the gas within, remain immiscible and the sharp interface between them retains its identity. The challenges encountered in the numerical treatment of such systems, especially in an accurate and robust capture of the interface when the impedance jump across it is large, were summarized in [1]. There we laid out a mixture-theory model in which the interface is regarded as an entity of finite but narrow width, extending to a few computational cells. Even though it is only within this thin

zone that the solid and the gas coexist, with one or the other of the constituents being absent everywhere else, the model extends the notion of the mixture to the entire computational domain. This allows the same set of governing equations to prevail everywhere. Closure conditions required by the mixture-theory treatment are chosen by considerations of numerical robustness rather than a faithful adherence to some preconceived physics of the interface. It is assumed, in particular, that certain constitutive parameters advect with the mixture, following similar formulations proposed by others; see Abgrall [11] and Saurel and Abgrall [12], for example.

The above model is extended in this study to accommodate the reactive solid, which itself is now treated as a homogeneous mixture of two distinct constituents, the unreacted explosive and the product of reaction. To each constituent is assigned an equation of state, and a single reaction-rate law (mentioned above) is postulated for the conversion of the reactant to product. It is assumed that the two constituents are in pressure equilibrium, that they travel with the same velocity, and that the conversion takes place without change in density. The internal energy of the solid mixture is the sum of the internal energies of the individual constituents, weighted by the reaction progress variable.

We note that while the formulation of advected parameters follows a similar approach used by others, our numerical treatment of the governing equations is different. The numerical approach used here follows that discussed in [13] for compressible two-phase flow and adjusted to multi-material flow in [1], and it is extended to accommodate the reactive solid. This extension uses a Strang-type fractional step scheme in which the nonlinear convective terms in the governing equations are advanced in one step (with the reaction-rate term set to zero), while the reaction term is integrated in the other step (with convection turned off). The overall approach is stable and second-order accurate (for regions of smooth flow), and is similar to that used by us for other reactive-flow problems, see [14, 15, 16, 17] for example. The numerical method uses adaptive mesh refinement (AMR) and is implemented in parallel, and it is available as part of the Overture framework of codes [18].

The paper is organized as follows. Section 2 introduces the configuration under study and the governing equations. The numerical approach is outlined in Section 3. Section 4 contains a detailed description of the various cases of cavity collapse and the subsequent evolution of reaction, culminating either in the development of a detonation or in a failure to detonate. Computational results are presented for incident shock of a given Mach number, for three different cavity shapes, and for four different choices of a parameter that can be viewed as measuring either the strength of the reaction rate or the size of the cavity. Concluding remarks are made in Section 5.

2 Model

The physical setup, shown in Figure 1, consists of an axisymmetric cavity filled with an inert gas and situated within a reactive solid in three-dimensional space. The initial state corresponds to a planar shock propagating in the unreacted solid from left to right and approaching the cavity. The jump in pressure across the shock is assumed to be large, allowing the shocked solid to be modeled as a compressible fluid, but not so large as to initiate reaction in the solid prior to the shock colliding with the cavity. (We shall retain the term 'solid' even though the material is modeled as a compressible fluid.)

2.1 Governing equations

The gas and the solid are separated by a sharp interface to begin with, and would remain so in the exact solution of the flow at later times. However, in our numerical approximation of the flow the interface is smeared initially over two or three grid cells, and the width of this smear can increase as the solution evolves according to our shock-capturing scheme. Within the smeared interface there exists a mixture of the gas and the solid, and the latter itself may be composed of the reactant and the product. Thus we are led to a mixture formulation of the governing equations, which is described below and is well suited for our numerical scheme (see Section 3). For the computational results described later, the diffuse-interface regions are thin and purely numerical, and we assign no particular physical significance to the behavior of the flow variables in such regions.

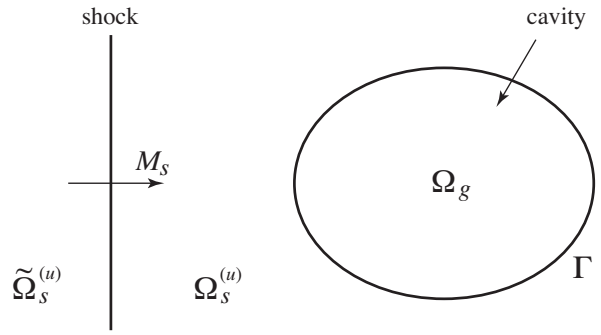

Figure 1: Initial configuration for shock-induced cavity collapse. Regions Ω_g, $\Omega_s^{(u)}$ and $\tilde{\Omega}_s^{(u)}$ denote the gas in the cavity, the unreacted solid ahead of the shock and the solid behind the shock, respectively. The Mach number of the incident planar shock is given by M_s, and Γ denotes the boundary of the cavity.

Surface tension forces, being small relative to the gasdynamic forces at the interface, are neglected. Viscosity and heat conduction are assumed to be negligible as well in both the solid and the gas so that the flow is governed by the Euler equations. In the axisymmetric geometry these equations are

$$\frac{\partial}{\partial t}\mathbf{u} + \frac{\partial}{\partial x}\mathbf{f} + \frac{\partial}{\partial y}\mathbf{g} = \mathbf{h}\,, \tag{1}$$

where

$$\mathbf{u} = \begin{bmatrix} \rho \\ \rho u \\ \rho v \\ \rho E \end{bmatrix}, \qquad \mathbf{f} = \begin{bmatrix} \rho u \\ \rho u^2 + p \\ \rho uv \\ u(\rho E + p) \end{bmatrix}, \qquad \mathbf{g} = \begin{bmatrix} \rho v \\ \rho uv \\ \rho v^2 + p \\ v(\rho E + p) \end{bmatrix}, \qquad \mathbf{h} = -\frac{v}{y}\begin{bmatrix} \rho \\ \rho u \\ \rho v \\ \rho E + p \end{bmatrix}.$$

Here, ρ, (u, v), p, and E denote the density, velocity, pressure and total energy of the mixture, respectively, at a position (x, y) and time t, with x being the axial coordinate and y the radial coordinate. The total energy is defined as

$$E = e + \frac{1}{2}\left(u^2 + v^2\right)\,,$$

where the internal energy e is prescribed by a stiffened-gas equation of state for the mixture of the form

$$e = \frac{p + \gamma\pi}{(\gamma - 1)\rho} - \lambda q\,, \tag{2}$$

where γ is the polytropic exponent, π the stiffening pressure, λ the progress of reaction, and q the heat release.

The conservation equations in (1) are augmented by a set of advection equations for the constitutive properties of the components comprising the mixture. This approach, introduced by Abgrall [11] and later extended by Saurel and Abgrall [12] and by us [1], provides a robust means of capturing interfaces without the appearance of spurious oscillations, and was successfully employed in our earlier study of inert cavity collapse where advection was applied to γ and π. Here this procedure is extended further by designating additional quantities for advection in recognition of the fact that the solid, upon reaction, will itself consist of two distinct components, the unreacted material and the reaction product. Thus the new advection equations are

$$\frac{\partial}{\partial t}\mathbf{z} + u\frac{\partial}{\partial x}\mathbf{z} + v\frac{\partial}{\partial y}\mathbf{z} = \mathbf{k}\,, \tag{3}$$

where

$$\mathbf{z} = \begin{bmatrix} \lambda \\ \mathbf{w}^{(u)} \\ \mathbf{w}^{(r)} \\ q \end{bmatrix}, \qquad \mathbf{k} = \begin{bmatrix} \mathcal{R} \\ 0 \\ 0 \\ 0 \end{bmatrix} .$$

Here $\mathcal{R}$ is the reaction rate, $\mathbf{w}^{(u)}$ and $\mathbf{w}^{(r)}$ to be defined below are vectors carrying the constitutive properties of the components of the mixture, and q is assigned to be the heat released by the reaction. The reaction rate assumes first-order, pressure-dependent kinetics, given by

$$\mathcal{R} = \begin{cases} \sigma(1-\lambda)(p - p_{\text{ign}}) & \text{if } p > p_{\text{ign}} \ , \\ 0 & \text{otherwise} \ , \end{cases} \tag{4}$$

where σ is the reaction prefactor and p_{ign} is the ignition-pressure threshold. The vector $\mathbf{w}^{(i)}$, $i = u$ or r, is defined as

$$\mathbf{w}^{(i)} = \begin{bmatrix} \dfrac{1}{\gamma^{(i)} - 1} \\ \dfrac{\gamma^{(i)} \pi^{(i)}}{\gamma^{(i)} - 1} \end{bmatrix} .$$

The components of $\mathbf{w}^{(i)}$ take the values corresponding to the unreacted solid (for $i = u$) or the reaction product (for $i = r$) on the solid side of the interface, and those corresponding to the gas on the gas side of the interface, with a smooth variation within the interface. The variable q takes the nonzero value of the heat release in the solid and is zero in the gas, with a smooth variation through the interface. Upon using the advected quantities given in (3), the equation of state for the mixture in (2) becomes

$$e = \frac{w_1 p + w_2}{\rho} - \lambda q \ , \tag{5}$$

where now, $\mathbf{w}$ is simply the λ-weighted sum of the corresponding vectors for the constituents,

$$\mathbf{w} = \begin{bmatrix} w_1 \\ \\ w_2 \end{bmatrix} = (1-\lambda)\mathbf{w}^{(u)} + \lambda \mathbf{w}^{(r)} \ .$$

Equations (1) and (3), along with the rate equation (4) and the mixture equation of state (5), constitute the full set of governing equations.

We remark that the reaction progress λ, heat release variable q and constitutive variables $\mathbf{w}^{(u)}$ and $\mathbf{w}^{(r)}$ are defined throughout the problem domain, including the region occupied by the inert gas. This is done for numerical convenience. For the gas, we set $q = 0$ and $\mathbf{w}^{(u)} = \mathbf{w}^{(r)}$, and the value of λ has no significance since there is no heat to be released by reaction.

Returning to Figure 1, the incident shock travels to the right, with Mach number M_s, into the undisturbed solid at rest in the region $\Omega_s^{(u)}$. The density and pressure of the solid in this region are given by ρ_s and p_s respectively. The state of the unreacted solid in the region $\tilde{\Omega}_s^{(u)}$ behind the shock is determined by the normal shock conditions, i.e.,

$$\frac{\tilde{\rho}_s}{\rho_s} = \frac{(\gamma_s^{(u)} + 1) M_s^2}{(\gamma_s^{(u)} - 1) M_s^2 + 2}, \qquad \frac{\tilde{u}_s}{c_s} = \frac{2(M_s^2 - 1)}{(\gamma_s^{(u)} + 1) M_s}, \qquad \frac{\tilde{p}_s - p_s}{p_s + \pi_s^{(u)}} = \frac{2\gamma_s^{(u)}(M_s^2 - 1)}{\gamma_s^{(u)} + 1}, \tag{6}$$

where c_s is the sound speed in the undisturbed solid. As indicated earlier, the post-shock pressure $\tilde{p}_s$ does not exceed p_{ign} so that the solid remains unreacted, and hence the values of γ_s and π_s appearing in the above expressions carry the superscript u. The initial state of the gas in region Ω_g inside the cavity is taken to be at rest, with density and pressure given by ρ_g and p_g, respectively. The polytropic exponent and the stiffening pressure for the gas are γ_g and π_g, with the latter quantity taken to be zero. Finally, it is assumed that the gas inside the cavity and the solid surrounding it are in mechanical and thermal equilibrium across the interface Γ, a contact discontinuity, that forms the boundary of the cavity at $t = 0$.

2.2 EOS parameters, ambient state, and nondimensionalization

The ambient state in the gas within the cavity and the surrounding solid is taken to be

$$\rho_g = 1.161 \text{ kg/m}^3, \qquad p_g = 10^5 \text{ Pa},$$
$$\rho_s = 1905. \text{ kg/m}^3, \qquad p_s = 10^5 \text{ Pa}.$$

These values are consistent with an air-filled cavity and a typical HMX-type explosive solid at standard atmospheric pressure and temperature. The parameters for the equation of state of the gas are prescribed by

$$\gamma_g = 1.4, \qquad \pi_g = 0, \qquad q_g = 0,$$

while the parameters for the unreacted and reacted solid are prescribed by

$$\gamma_s^{(u)} = 5.0, \qquad \pi_s^{(u)} = 6.858 \times 10^8 \text{ Pa}, \qquad q_s^{(u)} = 5.5 \times 10^6 \text{ J/kg},$$

and

$$\gamma_s^{(r)} = 2.0, \qquad \pi_s^{(r)} = 0, \qquad q_s^{(r)} = 5.5 \times 10^6 \text{ J/kg},$$

respectively. The sound speeds of the gas and solid in the undisturbed regions are

$$c_g = \sqrt{\gamma_g p_g/\rho_g} = 347.2 \text{ m/s}, \qquad c_s = \sqrt{\gamma_s^{(u)}(p_s + \pi_s^{(u)})/\rho_s} = 1342. \text{ m/s},$$

respectively. The initial state of the flow behind the shock is determined by the shock Mach number and the jump conditions in (6). For the calculations in this paper, we consider $M_s = 2.0$. The corresponding speed of the shock in the solid is

$$D_s = c_s M_s = 2684. \text{ m/s},$$

while the state behind the shock is given by

$$\tilde{\rho}_s = 2540. \text{ kg/m}^3, \qquad \tilde{u}_s = 670.9 \text{ m/s}, \qquad \tilde{p}_s = 3.430 \times 10^9 \text{ Pa}. \tag{7}$$

The governing equations are made dimensionless by choosing suitable reference scales for the problem. The reference scale for velocity is taken to be the acoustic speed in the undisturbed gas, and that for pressure the standard atmospheric pressure. Thus we have

$$u_{\text{ref}} = c_g = 347.2 \text{ m/s}, \qquad p_{\text{ref}} = p_g = 10^5 \text{ Pa},$$

and from these we compute the reference density,

$$\rho_{\text{ref}} = p_{\text{ref}}/u_{\text{ref}}^2 = 0.8295 \text{ kg/m}^3.$$

The time scale is given by

$$t_{\text{ref}} = x_{\text{ref}}/u_{\text{ref}},$$

where x_{ref} is a reference length scale that we keep arbitrary for now. We define the dimensionless quantities $x' = x/x_{\text{ref}}$, $y' = y/x_{\text{ref}}$, $t' = t/t_{\text{ref}}$, $\rho' = \rho/\rho_{\text{ref}}$, etc., to convert the governing equations into a dimensionless form. There now appears the nondimensional group

$$\sigma' = \frac{\sigma\, p_{\text{ref}}\, x_{\text{ref}}}{u_{\text{ref}}}$$

as the premultiplier in the dimensionless version of the rate equation (4). Otherwise the resulting equations have the same form as the original set, and thus the equations in (1), (3), (4) and (5) may be viewed as dimensionless (with the primes on all variables dropped for notational convenience). The dimensionless quantities in the three regions of the initial configuration in Figure 1 are collected in Table 1. In the expression for the reaction rate, p_{ign} is taken to have the dimensionless value 10^5, and σ is assumed to lie in the range $[0.001\,,\, 0.01]$.

Region	Ω_g	$\Omega_s^{(u)}$	$\tilde{\Omega}_s^{(u)}$
density, ρ	1.4	2296.	3062.
velocity, (u, v)	$(0, 0)$	$(0, 0)$	$(1.932, 0)$
pressure, p	1.0	1.0	34296.
EOS, (w_1, w_2)	$(2.5, 0)$	$(0.25, 8572.)$	$(0.25, 8572.)$
heat release, q	0	45.63	45.63

Table 1: Dimensionless initial states in the undisturbed gas (region Ω_g) and solid (region $\Omega_s^{(u)}$), and in the post-shock solid for $M_s = 2.0$ (region $\tilde{\Omega}_s^{(u)}$).

We now turn to the selection of the reference length. Consider a Chapman-Jouguet (CJ) detonation for which the upstream state is the post-shock state behind the Mach 2.0 incident shock, defined in (7). The thickness $x_{\rm rz}$ of the reaction zone in this CJ detonation is an intrinsic length in the problem. Equation (27) in the Appendix shows that the reaction-zone thickness, the reference length and the dimensionless reaction-rate prefactor σ are related by

$$\frac{x_{\rm ref}}{x_{\rm rz}} = 5000\,\sigma. \tag{8}$$

If $x_{\rm rz}$ is considered as a given quantity for a particular explosive, then the choice of σ defines the reference length $x_{\rm ref}$, and hence the size of the cavity being considered. (As we shall see in the section 4, each cavity shape that was investigated has a volume equivalent to that of a sphere of diameter 0.4 dimensionless units.) Our choice of allowing σ to be in the range $[0.001\,,\,0.01]$ corresponds to cavity diameter varying from twice to twenty times the reaction-zone thickness. Alternatively, if $x_{\rm ref}$ is prescribed to be a characteristic cavity size, then the choice of σ corresponds to the selection of a reaction rate (and hence the selection of the explosive), and the above equation then defines the corresponding reaction-zone thickness.

3 Numerical method

In this section, we describe the numerical method employed to obtain well-resolved solutions of the governing equations for different cavity configurations and for different values of the reaction pre-factor σ which, as discussed in the previous section, provides a measure of the size of the cavity. A Strang-type fractional-step scheme is used to advance the equations in time. One step handles the nonlinear convection portion of the equations with the reaction rate set to zero (but with the geometric source term retained), while the other step considers the reaction rate alone. A high-resolution Godunov method is employed for the nonlinear-convection step so that shocks and contact discontinuities (including the interface between the gas and solid) are captured in the numerical solution, while the reaction zone behind the leading shock of a detonation is resolved on the grid. An exact Riemann solver is used to compute the (conservative) flux functions in the Godunov method and to advance the constitutive variables in (3) following the approach described in [1], which extends the work in [13, 19]. We have found that more accurate results for the cavity problems considered here are obtained using an exact Riemann solver in comparison to results obtained using an approximate Riemann solver, such as an HLLC solver [20], which requires less computational cost per time step. The choice of the constitutive variables in (3) and the discretization of these advection equations is often guided by the property that uniform pressure-velocity (UPV) flow is maintained, and this is done so that oscillations in the pressure near the interface are suppressed (see [12], for example). The numerical approach used here is not guided directly by this property, but rather UPV flow is maintained as a consequence of the numerical approximation as was discussed in [1]. Finally, the numerical method discussed in this section is part of the Overture set of codes (see Acknowledgements), and is implemented in parallel using adaptive mesh refinement (AMR) following the work in [14] and [21].

3.1 Fractional step scheme

The numerical solution of the cavity problem shown in Figure 1 is computed on a uniform grid with spacings Δx and Δy in the x and y directions, respectively. Let $\mathbf{U}^n_{i,j}$ and $\mathbf{Z}^n_{i,j}$ denote approximations of $\mathbf{u}(x,y,t)$ and $\mathbf{z}(x,y,t)$ at a grid cell (x_i, y_j) and a time t_n. These grid functions are advanced in time using the fractional-step scheme

$$\mathbf{Q}^{n+1}_{i,j} = \mathcal{S}_k(\Delta t/2)\, \mathcal{S}_h(\Delta t)\, \mathcal{S}_k(\Delta t/2)\, \mathbf{Q}^n_{i,j},$$

where $\mathbf{Q}^n_{i,j} = (\mathbf{U}^n_{i,j}, \mathbf{Z}^n_{i,j})$ and Δt is the time step from t_n to t_{n+1} (chosen to satisfy a CFL stability condition). The operators $\mathcal{S}_h(\tau)$ and $\mathcal{S}_k(\tau)$ represent numerical integrations of the equations

$$\left.\begin{aligned} \frac{\partial}{\partial t}\mathbf{u} + \frac{\partial}{\partial x}\mathbf{f} + \frac{\partial}{\partial y}\mathbf{g} &= \mathbf{h} \\ \frac{\partial}{\partial t}\mathbf{z} + u\frac{\partial}{\partial x}\mathbf{z} + v\frac{\partial}{\partial y}\mathbf{z} &= 0 \end{aligned}\right\}, \tag{9}$$

and

$$\left.\begin{aligned} \frac{\partial}{\partial t}\mathbf{u} &= 0 \\ \frac{\partial}{\partial t}\mathbf{z} &= \mathbf{k} \end{aligned}\right\}, \tag{10}$$

respectively, over a time interval τ. The numerical integration of the hyperbolic system in (9) follows directly from the approach for the equations governing the behavior of the inert cavity discussed in [1], and we will not repeat the description here. The equations in (10) reduce to the ODE

$$\frac{\partial \lambda}{\partial t} = \mathcal{R}, \tag{11}$$

with ρ, (u,v), E, $\mathbf{w}^{(i)}$, and q held fixed. The mixture pressure p in $\mathcal{R}$ may then be obtained in terms of λ and the aforementioned fixed quantities from the mixture equation of state in (5). The numerical integration of (11) uses a second-order Runge-Kutta (RK) error-control scheme following the approach discussed in [14] and [16], for example.

The numerical approach for multi-material reactive flow as described above is performed in parallel using AMR. A uniform grid at the base level covers the domain of interest, and block-structured refinement grids are built on top of this uniform grid according to an error estimator so that sharp features of the flow, such as shocks and contact discontinuities (including the interface), are computed on the finest grid level. In regions of the flow where reaction is significant, such as the reaction zone of a detonation, the grid is refined according to the error estimate used in the RK error-control scheme (see [14] for further details). The grid cells are refined by a factor of $n_r = 4$ in each coordinate direction and n_ℓ refinement grid levels are allowed in the AMR hierarchy. Typically, we use $n_\ell = 1$ or 2. All grids, including the base-level grid and its refinement grids, may be partitioned and assigned to a set of processors, so that the calculations are done in parallel. The assignment is made according to a load-balancing algorithm as described in [21]. We generally use 32 processors for the numerical calculations presented later in this paper.

3.2 Grid convergence

Several tests were discussed in [1] to verify the accuracy of the numerical method in the context of inert multi-material flow. In particular, second-order accuracy of the numerical method for smooth flow was established using the method of analytical solutions, and self-convergence studies were performed for flows involving the interaction of a shock and a gas-solid interface. For the latter case, it was shown that the position of the interface was obtained accurately without numerical oscillations in the state variables on either side of it. Analogous tests involving the present model of reactive multi-material flow give similar results, and thus they are not described here. Instead, we focus attention on a particular test involving a representative flow in which there is significant reaction in the solid.

The initial conditions for the one-dimensional test flow at $t = 0$ involve an unreacted solid at rest for $x > 0.5$ and an unreacted solid for $x < 0.5$ moving to the right with speed V_0. The one-dimensional flow is

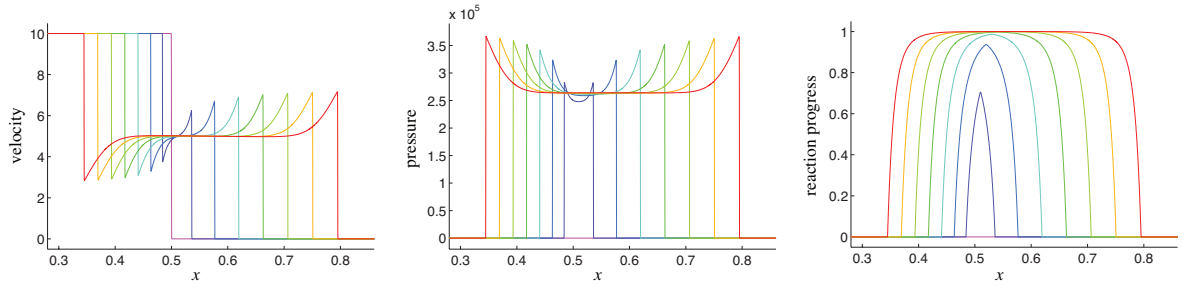

Figure 2: Reactive solid-solid collision: Velocity (left), pressure (middle) and reaction progress (right) for times $t = 0 : 0.002 : 0.014$.

a model for the collapse of a gas cavity at the moment the jetting face of one side of the cavity collides with the stationary face of the cavity on the other side. Such a solid-solid collision gives rise to high pressures and can lead to significant reaction in the reactive solid. Using the dimensionless parameters discussed in Section 2.2 and listed in Table 1, we set

$$\rho = 2296., \qquad p = 1.0, \qquad \lambda = 0, \qquad w_1 = 0.25, \qquad w_2 = 8572., \qquad q = 45.63,$$

for the solid occupying all x at $t = 0$, and set

$$u = \begin{cases} 10 & \text{if } x < 0.5, \\ 0 & \text{if } x > 0.5. \end{cases}$$

The choice $V_0 = 10$ is suggested by the typical (dimensionless) velocity observed at the moment of first collapse of the spherical cavity considered in detail in the next section. The reaction prefactor σ in (4) is taken to be 0.005 , corresponding to the base value among the choices discussed later, and the ignition-pressure threshold is set to be $p_{\text{ign}} = 10^5$.

Figure 2 shows the behavior of the velocity, pressure and the reaction progress for $t = 0 : 0.002 : 0.014$. The collision of the solid on the left with the solid at rest on the right produces a blast region in which the pressure exceeds p_{ign}, thereby initiating the reaction. Two shocks are generated by the initial impact, one traveling to the right into the solid at rest and the other traveling to the left into the right-moving solid. These shocks bound the blast region, are strengthened by the reaction behind them, and ultimately transition into detonations.

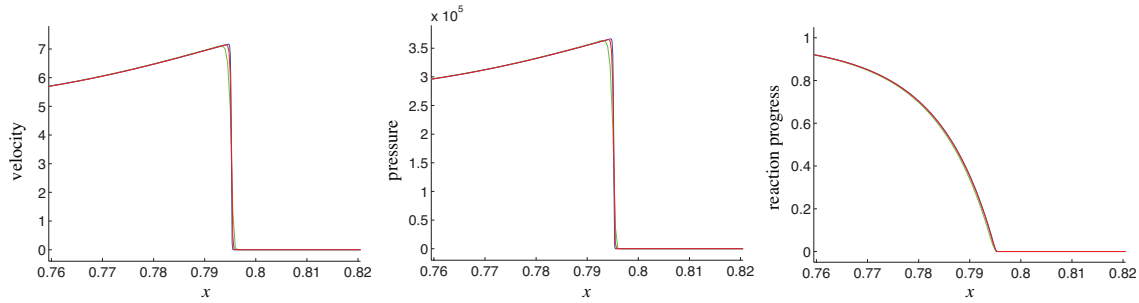

Figure 3: Reactive solid-solid collision: Enlarged views of velocity (left), pressure (middle) and reaction progress (right) near the right-traveling detonation at $t = 0.014$ computed using grids with $\Delta x = 1/2000$ (green), 1/4000 (red) and 1/8000 (blue).

For this flow, we consider solutions computed on grids with three different values of the grid spacing Δx to illustrate the accuracy of the numerical method. Figure 3 shows enlarged views of the solution at

$t = 0.014$ near the right-traveling detonation for grids with $\Delta x = 1/2000$ (green), 1/4000 (red) and 1/8000 (blue). The solution curves lie very close to one another for each grid, with the only noticable difference occuring near the shock indicating excellent accuracy of the computed solutions. All of the main results of the paper, discussed in the next section, use grids with $\Delta x = 1/4000$.

4 Numerical Results

We now describe in detail the principal features of the flow resulting from the collision between the incident shock originating in the solid and the gas-filled cavity embedded in the solid. The geometry of the configuration is displayed in Figure 4, which shows one-half of a symmetric cross-sectional view. The ellipsoidal cavity has semi-axes a and b initially and is centered at the origin of the coordinate system. The shock in the solid is located at $x = -s$ at $t = 0$, and moves to the right with a velocity determined by the shock Mach number $M_s = 2$. The base grid covers the numerical domain $-L \le x \le L$ and $0 \le y \le H$ with axis of symmetry $y = 0$. Three different cavity shapes are considered: sphere, prolate spheroid and oblate spheroid. The spherical cavity has dimensions $b = a = 0.2$. The spheroids are assigned the same volume as the sphere, but for each the major axis is twice as long as the minor axis.

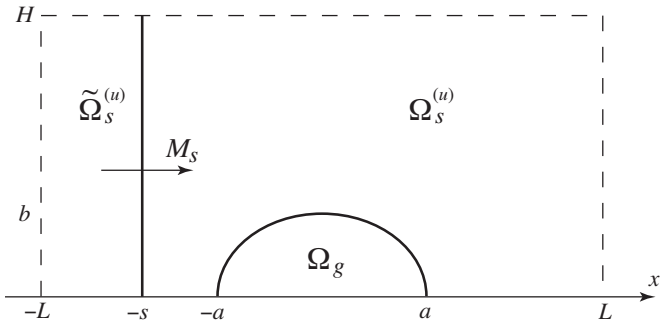

Figure 4: Domain for shock-induced collapse of an ellipsoidal cavity. The ellipsoidal cavity is centered at the origin and has semi-axes a and b. The shock is located in the unreacted solid at $x = -s$ initially. The base grid covers the domain $-L \le x \le L$ and $0 \le y \le H$ with axis of symmetry $y = 0$.

The computational results, presented below, are grouped by cavity shape. For the spherical cavity, four different choices of the reaction-rate prefactor are considered, namely, $\sigma = 0.001$, 0.0025, 0.005 and 0.01. For the prolate and oblate spheroids, results are presented for $\sigma = 0.001$, 0.005 and 0.01 only. The fourth value $\sigma = 0.0025$ was also examined for these latter two cavity shapes but the results were found to be close to those of the $\sigma = 0.005$ case and therefore omitted. As already mentioned, increasing σ may be considered as increasing the size of the cavity or strengthening the rate of reaction. The choice $\sigma = 0.005$ is viewed as the *base case*, for which fine details of the process of evolution are described. The descriptions are briefer for the other choices of σ. Shaded contour plots and on-axis profiles of pressure p and extent of reaction λ at various times are employed as descriptors of events. Due to axisymmetry of the cavity shape only the upper half of the cavity is displayed in each case. The terms 'horizontal' and 'vertical' are used to refer, respectively, to directions along, and normal to, the axis of symmetry, while 'up' and 'down' refer, respectively, to directions radially outwards or inwards. At time $t = 0$ the Mach 2.0 planar shock is incident at the front face of the cavity along the axis of symmetry. For the inert case, a full discussion of the events following the impact for each cavity shape appears in our earlier study [1]. Here, we show only a few plots of the events leading up to the instant when the impact of the front face of the cavity with the rear face has either just occurred or is imminent. For ease of interpretation and to focus attention on the solid, the cavity region is masked out in the contour plots. We recall from Table 1 that the dimensionless post-shock pressure is 3.43×10^4 units while the pressure threshold for ignition is 10^5 units.

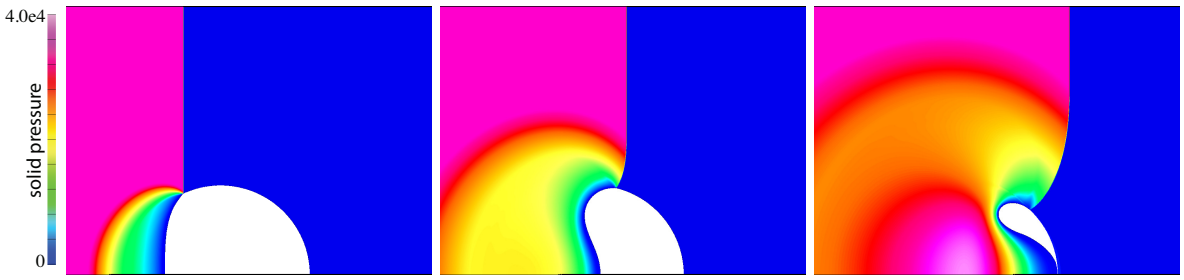

Figure 5: Spherical cavity: shaded contours of pressure p at times $t = 0.028,\ 0.048$ and 0.068 (left to right). Reaction has not yet begun, and collision between the solid jet and rear faces of the cavity is imminent at $t = 0.068$.

4.1 The spherical cavity

We begin with a discussion of the case of a spherical cavity. Figure 5 shows the interaction of the planar shock with the cavity at three early times, $t = 0.028,\ 0.048$ and 0.068, before any reaction occurs. The impact of the shock with the leading face of the cavity generates a reflected wave in the form of a rarefaction back into the solid and a transmitted shock in the gas. The latter wave is not shown in the blanked out region of the gas inside the cavity, but is well described in [1]. The oblique pressure gradient set up within the rarefaction causes the parallel flow entering the rarefaction front to converge towards the axis, thereby forming a high-speed jet traveling from left to right. The jet pushes on the front surface of the cavity, causing it to flatten ($t = 0.028$) and then to fold inwards ($t = 0.048$). At $t = 0.068$ the front face of the cavity is on the verge of colliding with the rear face. The cavity has thus been distorted into an approximately hemispherical bowl whose thickness diminishes from rim to base. The maximum pressure, located on the axis upstream of the front face of the cavity, is below the ignition threshold $p_{\rm ign}$, confirming that reaction has not yet begun.

4.1.1 Spherical cavity, $\sigma = 0.005$

We consider the sequence of events for the base case in three distinct stages.

Stage I. Figure 6 displays the contour plots and on-axis profiles of pressure and reaction progress at three selected times at this early stage. At $t = 0.072$ the front face has already slammed into the rear face, thereby punching an axial bore through the cavity and collapsing the cavity into a toroid whose cross section is in the shape of a teardrop. The impact has also generated a pair of oppositely traveling shock waves which enclose an expanding disk of high pressure (heretofore dubbed as the blast region) with a wedge-shaped semi-cross section. Of the two shocks bounding the blast, the one proceeding rightwards (the R-shock) is the weaker; it advances downstream into the stationary solid and retains the convex shape it possessed at the beginning of the impact. The leftward-bound shock (L-shock) advances upstream against the oncoming jet of solid reactant; its original concave profile has flattened out and even acquired a slightly convex bulge near the axis. In the entire blast domain the pressure is highest on the axis with the peak occurring at the L-shock, as is evident in the on-axis pressure plot in Figure 6. At 1.6e5 dimensionless units this pressure exceeds the ignition threshold, and in fact, $p > p_{\rm ign}$ on the axis nearly everywhere in the blast region where the reaction is thereby switched on; the exception being a narrow layer just behind the R-shock. The extent of reaction λ appears in the on-axis plot as a pulse with a peak of 0.23.

At $t = 0.076$ the blast region continues to expand, the L-shock now has a fully convex profile, the R-shock has begun to climb up the rear face of the cavity while the incident shock descends further down the same face. In the absence of reaction one may expect both the bounding shocks to weaken (as was seen in [1]) but here, both have gained strength due to the support provided by the reaction, the L-shock more so than the R-shock. Due to the higher pressure at the L-shock (2.25e5 units) the reaction zone behind it is thinner than that behind the R-shock. The on-axis plot of reaction progress now has a taller peak at $\lambda = 0.66$.

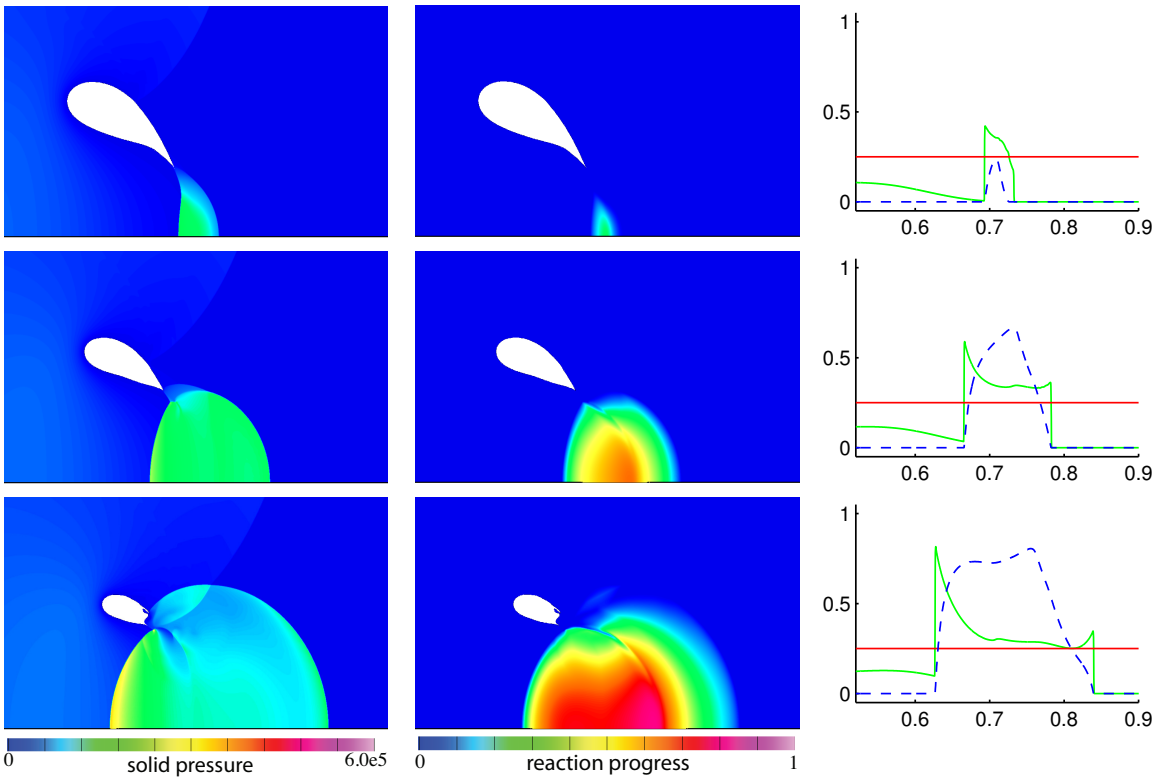

Figure 6: Spherical cavity, $\sigma = 0.005$, Stage I. The panels show shaded contours of p (left), λ (middle) and on-axis profiles (right) at times $t = 0.072$, 0.076 and 0.080 (top to bottom). The on-axis plots show $p/4.0e5$ in green, λ in blue and $p_{\rm ign}/4.0e5$ in red.

At $t = 0.080$ the expansion of the blast region, the contraction of the cavity and the strengthening of the L-shock, all continue. The on-axis pressure behind the L-shock has now risen to 3.4e5 units. The R-shock, on the other hand, suffers a slight drop in pressure at the axis, having lost the battle due to expansion against insufficient reactive support. Advancing up from the axis, the pressure at the R-shock remains roughly constant, declines somewhat near its apex, and rises again where the R-shock has now run into the incident shock along the rear wall of the cavity. Pressure throughout most of the blast is still above the ignition threshold, so that reactant consumption continues and on axis, λ has attained a peak value of 0.8. The reaction zone on the right is now substantially wider than that on the left. Finally, the uneven pressure along the rear wall of the cavity has caused it to fold back upon itself near the tip of the teardrop.

Stage II. Figure 7 displays the contour plots and the on-axis profiles of pressure and reaction progress at three selected times in this middle stage. At $t = 0.084$ the cavity, in cross section, has just collapsed fully into a thin ribbon with a backward hook at its nose, a location towards which the L-shock and the R-shock are now converging. Weak pressure disturbances emanating from the cavity, including a relatively stronger one of spherical shape issuing from the nose of the cavity, are now visible in the plot of the pressure contours. (More about these disturbances, and about events occurring during the short time span bracketing the collapse, will follow shortly.) Along almost the entire length of the decaying R-shock the pressure has fallen below the ignition threshold, thereby extinguishing the reaction behind it. The on-axis plot of λ now exhibits twin peaks; the one on the left at level 0.88 is produced by the strong reaction behind the L-shock while the one on the right retains the level of 0.8 seen at the last time level of Stage I discussed above, confirming the fact that the reaction in this region is extinguished and that the peak has simply convected to its new location.

At $t = 0.088$ the L- and R-shocks, and the secondary blast created by the final collapse of the nose of the cavity, have interacted to generate a complex pattern in which the bulk of the L-shock acts as a

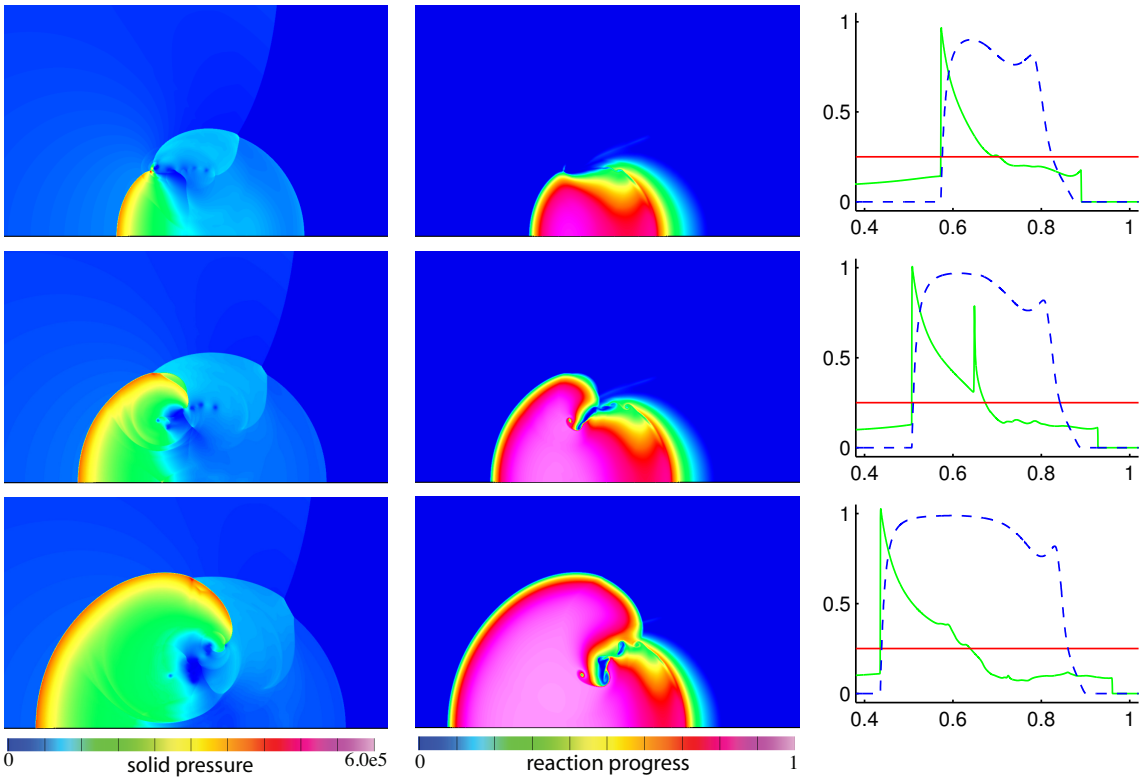

Figure 7: Spherical cavity, $\sigma = 0.005$, Stage II. The panels show shaded contours of p (left), λ (middle) and on-axis profiles (right) at times $t = 0.084$, 0.088 and 0.092 (top to bottom). The on-axis plots show $p/4.0e5$ in green, λ in blue and $p_{\rm ign}/4.0e5$ in red.

curved stem to the top of which is attached a claw, consisting of an expanding sequence of concentric shocks centered at the erstwhile cavity nose. One of the circular disturbances has just reflected off the axis, thereby generating a spike in the middle of the on-axis pressure plot. Along the axis the R-shock has continued to weaken, thereby widening the region of extinguished reaction behind it. A bulk of the extinguished region contains partially reacted solid, but immediately behind the R-shock there is now a layer in which the solid is completely unreacted. Behind the L-shock on the other hand, the thin reaction zone is followed by a broad region in which the reaction has nearly reached completion. The zone above the cavity processed by both the incident shock and the R-shock continues to grow.

At $t = 0.092$ the claw mentioned above has expanded, its upper arm now becoming an extension of the L-shock hooking to the right, and its lower arm, significantly weakened, reflecting off the axis. The L-shock can rightly be said to have transformed itself into a curved detonation with a hook at the top right, which is advancing into partially reacted material. The behavior at this stage is reminiscent of detonation diffraction at a 90° corner [15, 17, 19, 22]. The formation of a detonation hook that consumed partially reacted material was a common feature in these studies. For the present study, the reaction is nearly fully completed over a broad area of the blast region behind the detonation, and even in the portion where reaction was once initiated but has now been switched off, about 80% of the reaction has been completed.

We now turn to a closer examination of events surrounding the final collapse of the cavity. Figure 8 shows enlarged views of the contours of pressure and reaction progress at times just before ($t = 0.082$ and 0.083), just at ($t = 0.084$) and just after ($t = 0.0845$ and 0.085) the instant of final collapse. In this figure we have also included gray-scale numerical schlieren images which highlight shocks and contact lines where changes in density are large. At $t = 0.082$ we observe a detonation led by the L-shock traveling to the left and upwards towards the cavity, and the diffracting R-shock traveling to the left around the upper portion of the cavity. The R-shocks interacts with the rear face of the cavity in much the same way as the

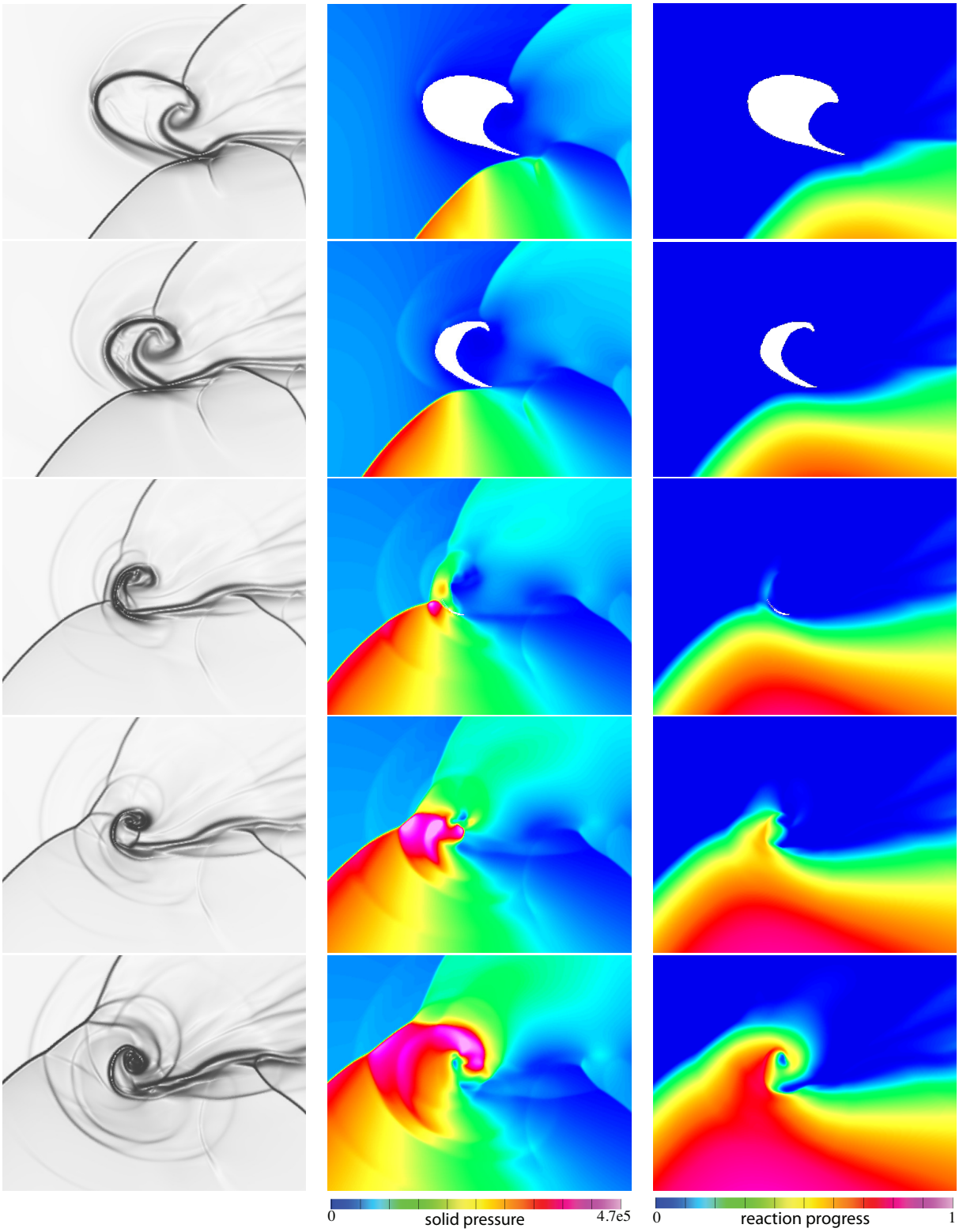

Figure 8: Spherical cavity, $\sigma = 0.005$, Stage II. Enlarged views showing the final collapse of the cavity and the creation of a secondary blast. The panels show shaded contours of numerical schlieren (left), p (middle) and λ (right) at times $t = 0.082$, 0.083, 0.084, 0.0845 and 0.085 (top to bottom).

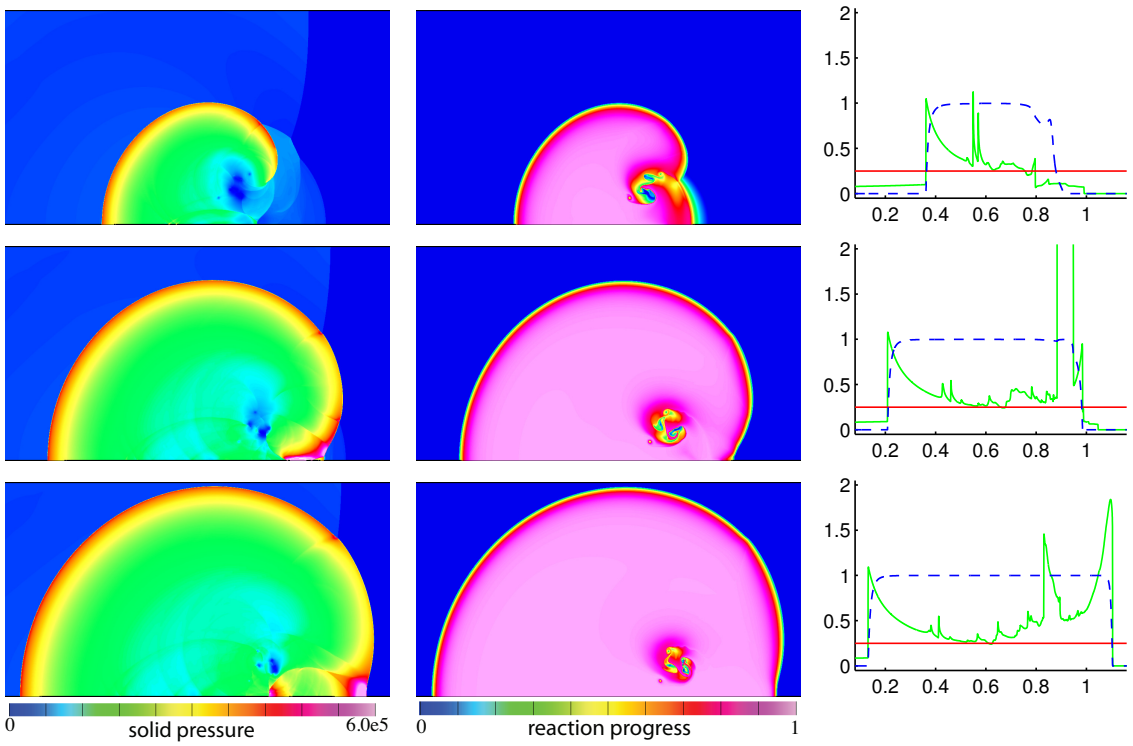

Figure 9: Spherical cavity, $\sigma = 0.005$, Stage III. The panels show shaded contours of p (left), λ (middle) and on-axis profiles (right) at times $t = 0.096$, 0.104 and 0.108 (top to bottom). The on-axis plots show $p/4.0e5$ in green, λ in blue and $p_{\rm ign}/4.0e5$ in red.

incident shock had done with the front face of the cavity, i.e., compressive waves traveling leftwards are transmitted into the cavity and a rarefaction traveling rightwards from the rear face of the cavity is reflected into the region traversed by the R-shock. A high-speed jet, traveling from right to left, propels the rear face of the cavity leftwards. Also visible in the pressure plot, and more prominently in the schlieren plot, is what appears to be a weak bow shock surrounding the cavity. This wave is simply the current manifestation of compressive disturbances generated at earlier times within the cavity and transmitted into the solid outside. At $t = 0.083$ the rear face of the cavity has edged closer to the front face and the 'bow shock' has moved away from the nose of the cavity. At $t = 0.084$ the cavity has fully collapsed, and the high-pressure blast resulting therefrom can be seen emerging from the nose of the cavity in the pressure and schlieren plots. We name this blast the secondary blast, to distinguish it from the primary blast seen in Stage I above. The pressure is particularly high, in fact higher than $p_{\rm ign}$, at the location where the secondary blast impacts the L-shock, resulting in a new site of chemical activity. A faint signature of the reaction at this site is visible in the reaction progress plot. At $t = 0.0845$ the blast continues to expand into the regions processed by the L and the R-shocks, with concomitant increase in pressure and hence reactant consumption. At $t = 0.85$ the blast, which has now developed into a detonation, hooks up and to the right into the previously unreacted region surrounding the nose of the collapsed cavity. The result is the claw-like structure alluded to above.

Stage III. Figure 9 displays the contour plots and on-axis profiles of pressure and reaction progress at three selected time levels in this late stage. Although the reflections off the axis have lent considerable noise to the on-axis pressure plots, the salient features are easily discerned. At $t = 0.096$ the lower arm of the aforementioned claw has reflected off the axis, while the detonation associated with the L-shock continues to advance. We note in particular the advance of the hook towards the R-shock on the right. At $t = 0.104$ the hook has overtaken the R-shock and also rammed into the axis, thereby generating two very sharp pressure peaks in the on-axis plot. We also see that the material within the blast is now fully reacted, save in a thin reaction zone behind the detonation. The exception are the remnants of the cavity material. At $t = 0.108$

the situation is unchanged, except that one of the sharp on-axis pressure peaks alluded to above has overtaken the R-shock, and the detonation has spread out further. It is clear that the period of significant transient evolution is over and that the detonation is now fully fledged.

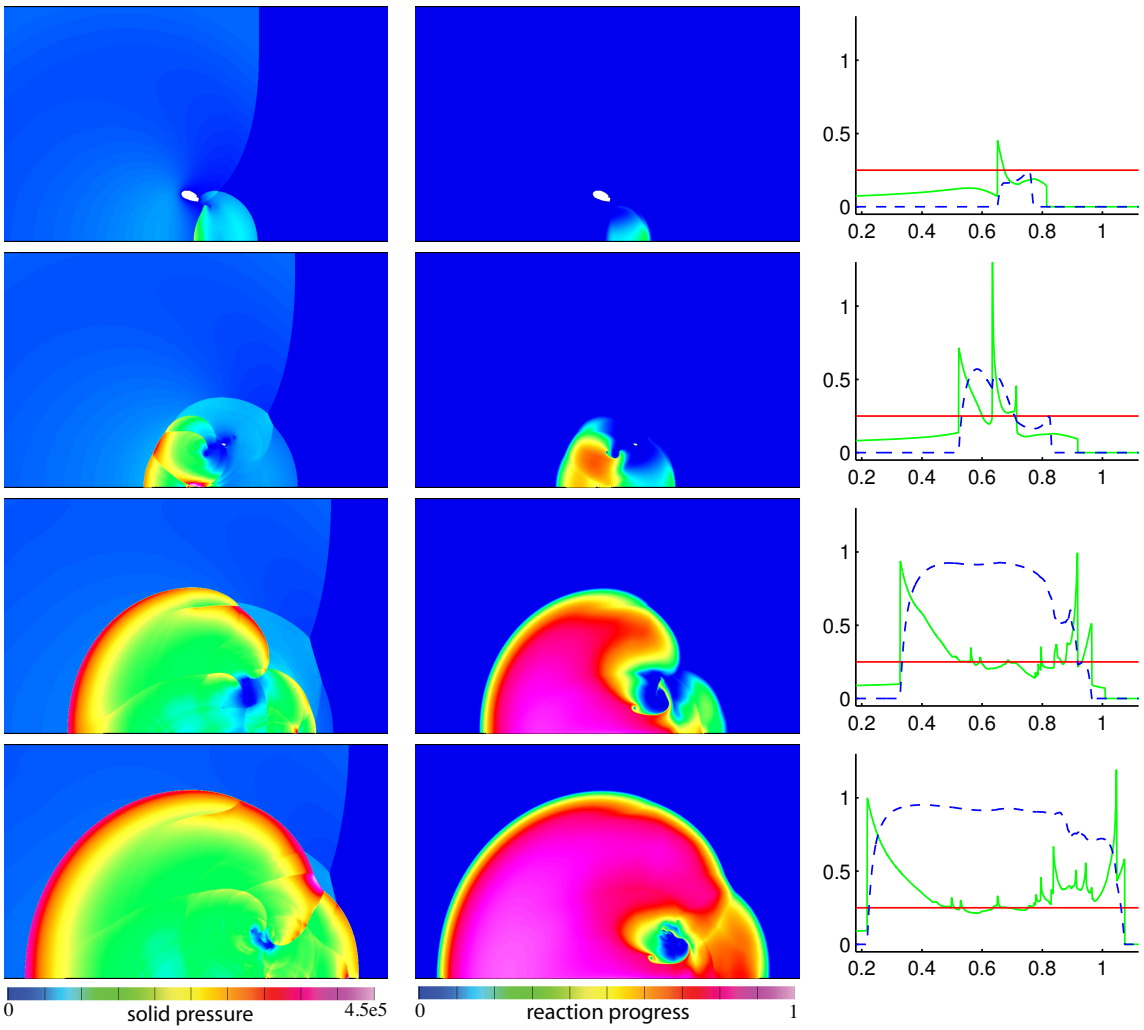

Figure 10: Spherical cavity, $\sigma = 0.0025$. The panels show shaded contours of p (left), λ (middle) and on-axis profiles (right) at times $t = 0.080$, 0.092, 0.104 and 0.110 (top to bottom). The on-axis plots show $p/4.0e5$ in green, λ in blue and $p_{\text{ign}}/4.0e5$ in red.

4.1.2 Spherical cavity, $\sigma = 0.0025$

With σ at half of the value of the base case, computations show that the scenario of detonation initiation has many basic features similar to that for $\sigma = 0.005$. There are some significant differences in the behavior, however, and these are illustrated in Figure 10 which shows the color contour plots and on-axis profiles at four selected instants in time.

At $t = 0.080$ the contour plots for pressure and reaction progress, when compared with those for the base case at the same time level (see Figure 6), reveal a picture that is qualitatively similar but quantitatively different. The expanding blast region, the contracting cavity, the strong L-shock and the weaker R-shock appear as before, but now the overall pressures are lower and the reaction has not progressed quite as far. The pressure, from the peak value of 1.8e5 units at the L-shock, declines sharply behind it and exceeds the ignition threshold only in a very narrow zone. Within this reaction zone λ rises rapidly to a peak of

0.16 and continues to rise gradually even in the region beyond to a second peak of 0.25, before declining to zero. The presence of partially reacted material outside the region where reaction is currently active is due to convection from the reaction zones of earlier times. Behind the R-shock there is a gap in which the material is completely unreacted, in contrast to the base case where the R-shock continues to act as a source of ignition immediately behind it. This shock has also crossed into the region behind the cavity through which the incident shock has already passed, thereby resulting in a slight increase in the local pressure but not enough to provoke a second ignition front.

At $t = 0.092$ the mutual interaction of the L- and R-shocks and the contributions from the spherical disturbances emanating from within the cavity, as discussed for the $\sigma = 0.005$ case above and shown in Figure 7, have again created the claw-like structure attached to the L-shock. For $\sigma = 0.0025$, the detonation is initiated from this later interaction, and not directly from the initial blast wave as was observed in the base case. The lower, curved edge of the claw structure has just undergone a head-on collision with the axis, thereby generating a new on-axis site of intense pressure, at level 7.6e5, and hence a commensurately strong reaction as well. As a result, the on-axis profile of λ now has three peaks, with the middle peak corresponding to the new reaction site. Further comparison with the base case at the same time level confirms the sustained weakness of the response, as reflected in the lower pressures, slower reaction progress, and the continuing absence of reaction behind the R-shock.

At $t = 0.104$ the L-shock has evolved into a nearly spherical detonation whose reach now extends beyond the apex of the blast region. The upper arm of the claw has evolved into a detonation of its own as well, which is advancing into the unreacted region downstream. A third shock-reaction complex, on the downstream side of the curved reflected shock mentioned above, is also gaining strength, and is responsible for the third of the four peaks in the on-axis λ plot. Even though a narrow zone behind the R-shock is still devoid of reaction, the reaction zone now does occupy nearly the entire blast domain on axis, and over a broad expanse of this zone the reaction has reached nearly full completion. A comparison with the corresponding plots for the base case, shown in Figure 9, finds that while the base case still exhibits a stronger response, the contrast between the two cases is now less pronounced.

At $t = 0.110$ the shock-reaction complex mentioned above has finally evolved into a detonation, and has pushed through the R-shock into the unreacted region beyond. In fact a merging of the various detonation segments has occurred, resulting in a nearly spherical expanding detonation. Outside the reaction zone the entire blast region is now nearly-fully occupied by reaction product, with the exception of a small void where surviving remnants of the inert cavity material exist. A comparison with the $t = 0.108$ plots for the base case, shown in Figure 9, indicates that the detonation, although fully developed, still exhibits slightly weaker pressure peaks at the on-axis detonation waveheads.

4.1.3 Spherical cavity, $\sigma = 0.01$

We now consider σ twice the size of that in the base case. Again it suffices to view the events at four selected times. The corresponding contour plots and on-axis profiles are displayed in Figure 11.

At $t = 0.076$ the contour plots for pressure and reaction progress, when compared with those for the base case at the same time level (see Figure 6), show a stronger post-collapse blast and the early establishment of a coupling between both the L- and R-shocks and the reaction. The reaction zone now covers the entire blast region and on axis, λ has already reached a peak value of unity. By $t = 0.080$ both shocks have evolved into detonations, with the one led by the L-shock being slightly stronger. At $t = 0.086$ the L- and the R-shocks have collided and the claw structure seen earlier has formed. The reflection of the lower contour of the claw with the axis has generated a local pressure peak. As the claw expands, there is little increase in its strength as it is propagating into regions that are already fully reacted. At $t = 0.088$ a fully developed detonation has emerged, and as it propagates, it leaves behind a small pocket of cavity material.

Unlike the smaller values of σ considered above, where the shock-reaction complex resulting from ignition due to the high post-collapse pressure tended to decay, at least behind the R-shock, and awaited such subsequent gasdynamic events as shock collision and shock reflection for its resuscitation and eventual transformation into a detonation, the shock-reaction coupling in the present case is immediate and sustained across the entire boundary of the blast, and a fully-formed detonation emerges rapidly.

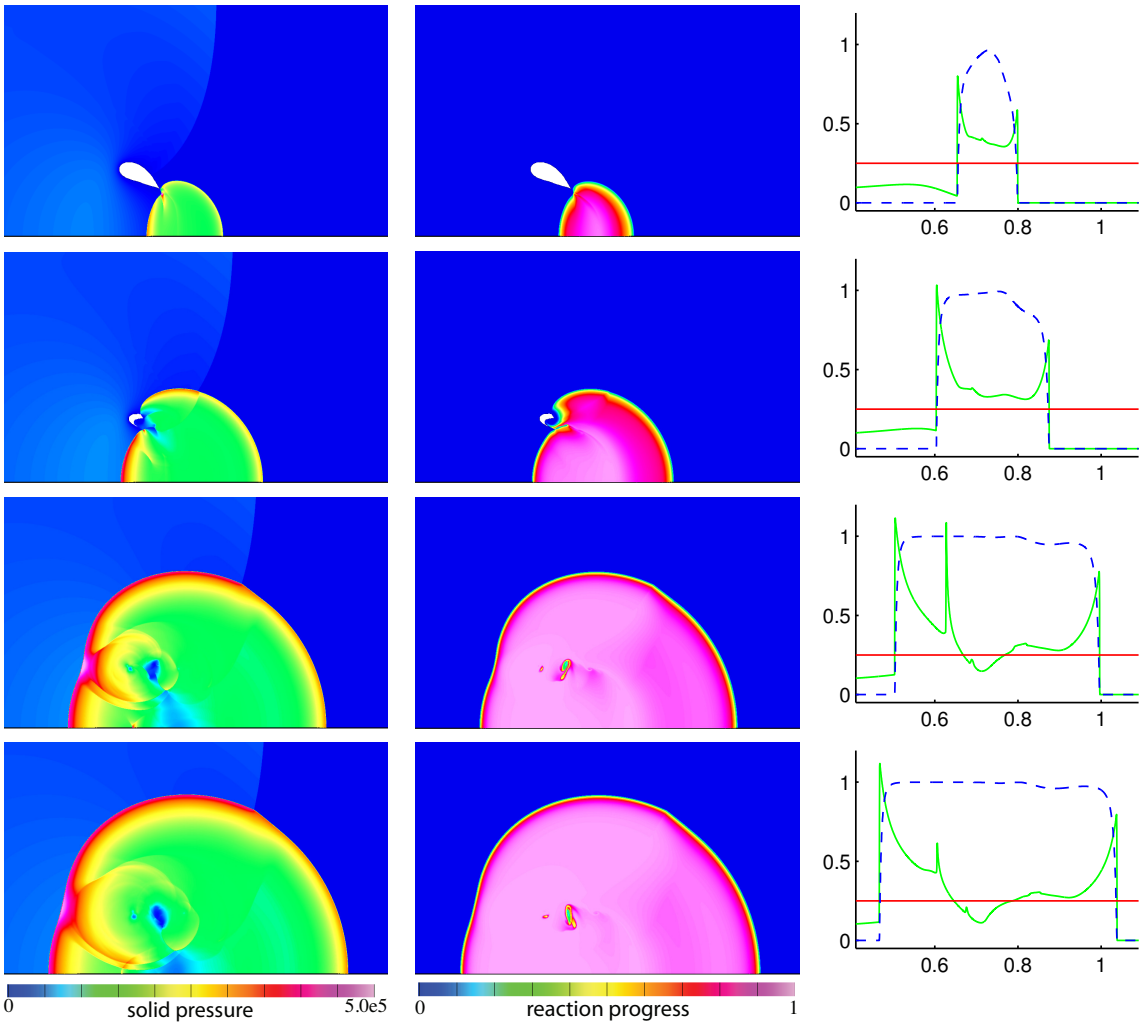

Figure 11: Spherical cavity, $\sigma = 0.01$. The panels show shaded contours of p (left), λ (middle) and on-axis profiles (right) at times $t = 0.076$, 0.080, 0.086 and 0.088 (top to bottom). The on-axis plots show $p/4.0e5$ in green, λ in blue and $p_{\text{ign}}/4.oe5$ in red.

4.1.4 Spherical cavity, $\sigma = 0.001$

As a last case, we consider a very small value of σ, one-fifth of the base-case value, to explore whether it is possible for a detonation to form. Four specific times are selected to view the evolutionary dynamics, and the corresponding contour plots and on-axis profiles are displayed in Figure 12.

At $t = 0.072$ the collapse generates a blast region as before but now the pressure exceeds the ignition threshold in an extremely thin zone behind the L-shock, as the on-axis plots clearly show. Correspondingly, progress of reaction is sluggish and λ is able to achieve a peak of only 0.05. As time progresses the R-shock wraps around the cavity to interact with the L-shock and a claw pattern forms as before. The plots at time $t = 0.096$ show that the lower contour of the claw has just reflected off the axis, thereby generating locally high pressures, as high as 4.2e5 units behind the L-shock, and lifting λ to a peak of 0.475. However, there is little evidence of a strong and sustained coupling between reaction and shock. By $t = 0.104$ the L-shock has decayed to a peak of 2.05e5 units on axis and the reaction zone behind it, though still in existence, has broadened. The peak value of λ is unchanged at 0.475 and is now located in a low-pressure region where reaction is no longer occurring. The plots at $t = 0.108$ indicate a further weakening of the L-shock and a corresponding decrease in reaction rate, and it is clear that the reaction is headed towards extinction

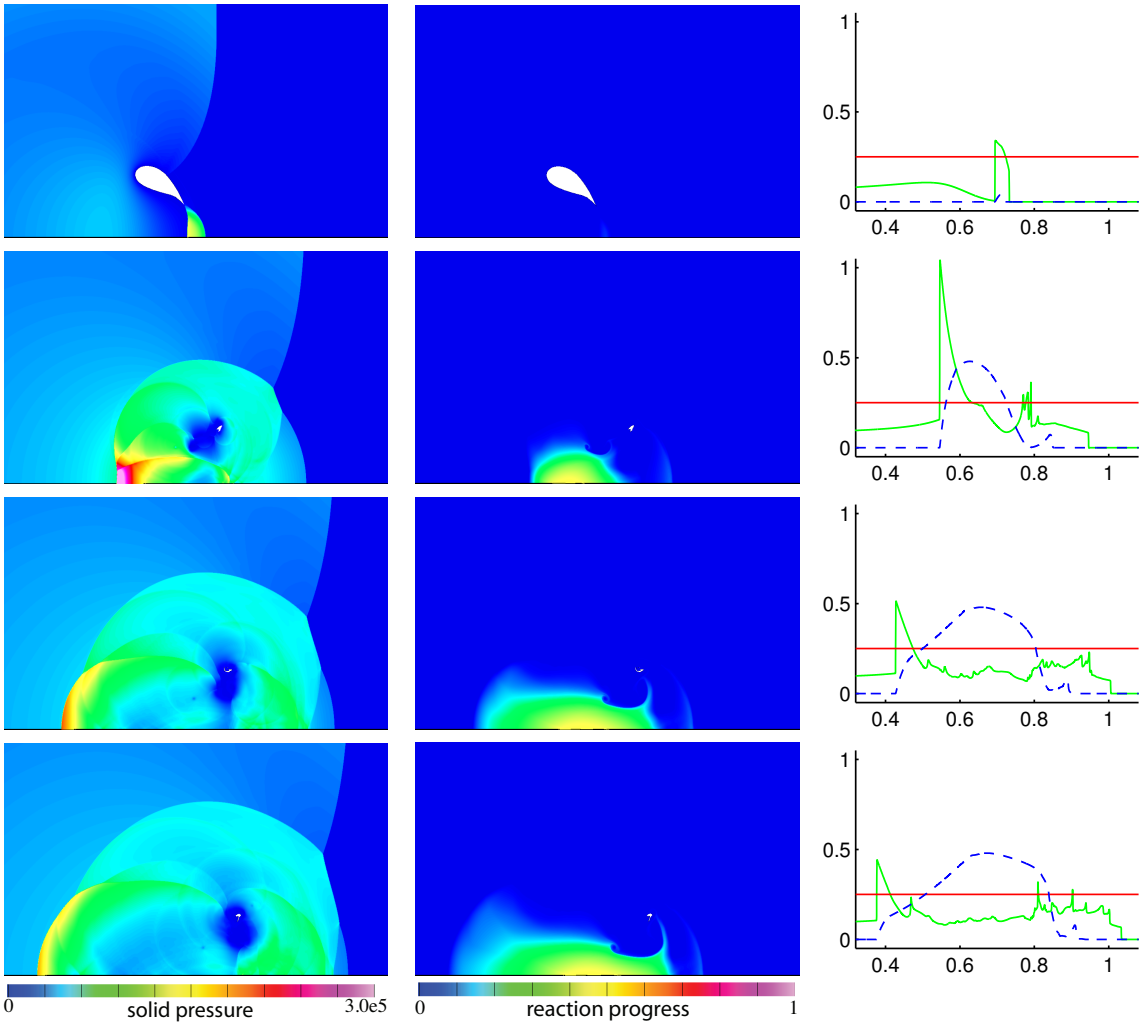

Figure 12: Spherical cavity, $\sigma = 0.001$. The panels show shaded contours of p (left), λ (middle) and on-axis profiles (right) at times $t = 0.072$, 0.096, 0.104 and 0.108 (top to bottom). The on-axis plots show $p/4.0e5$ in green, λ in blue and $p_{\rm ign}/4.0e5$ in red.

everywhere, leaving behind a parcel of partially reacted material.

4.2 The long ellipsoidal cavity

In this section, we examine the interaction of the incident shock with an ellipsoidal cavity in the shape of a prolate spheroid. For this case the major axis of the ellipsoid is twice as long as the minor axis, but the volume is the same as that of the spherical cavity considered in the previous section. The intent is to determine how the time and mode of evolution to detonation are affected by the shape of the cavity. Figure 13 shows the behavior of the solid pressure at three times after the initial impact of the planar incident shock, with Mach number $M_s = 2.0$ as before. At the earliest time shown, $t = 0.040$, we observe the diffracted leading shock traveling around the nose of the cavity, the reflected expansion wave ahead of the cavity, the indentation of the front face of the cavity, and the solid jet. At later times the jet advances along the axis. Due to the now longer distance between the cavity faces and the acceleration of the jet, the jet velocity is higher at the instant of collision of the two faces of the cavity as compared to the spherical case. This results in a somewhat stronger post-collision blast, imminent at $t = 0.088$, than was the case for the spherical cavity. However the maximum pressure, located on the axis upstream of the front face of the

cavity, is still below the ignition threshold p_{ign} for all times shown in the figure, so that reaction has not yet been initiated.

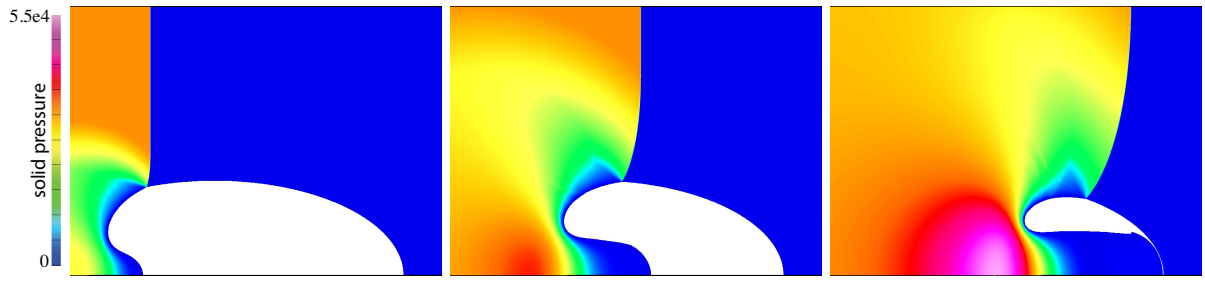

Figure 13: Long ellipsoidal cavity: shaded contours of pressure p at times $t = 0.040,\ 0.064$ and 0.088 (left to right). Reaction has not yet begun, and collision between the solid jet and rear face of the cavity is imminent at $t = 0.088$.

We consider the subsequent behavior for three values of σ in the subsections below, starting with the base case $\sigma = 0.005$ and then considering the cases $\sigma = 0.01$ and $\sigma = 0.001$.

4.2.1 Long cavity, $\sigma = 0.005$

For the base case, it is again convenient to examine the sequence of events in three distinct stages.

Stage I. Figure 14 displays the contour plots and on-axis profiles of p and λ at four selected times. At $t = 0.092$ the collision of the front and rear faces of the cavity has produced the blast region, with an L-shock that is stronger than the R-shock. Pressure within much of the blast (and on-axis throughout the blast) exceeds p_{ign} and initiates the reaction there. On the axis λ has achieved a peak value of 0.75. At $t = 0.098$ the blast has expanded and pressure within it has declined. Interaction of the L- and R-shocks with the tail of the cavity has generated pressure disturbances which are headed towards the axis. On the axis λ maintains the peak value of 0.75 and the pressure behind the R-shock has dropped to a value just below p_{ign}. At $t = 0.104$ the weakening of the blast continues, to the extent that the peak pressure is now found upstream of the blast. The R-shock has collided with the incident shock, and as the former travels up the rear face of the cavity it initiates a secondary collapse of the cavity in much the same way as was seen earlier for the spherical cavity. The aforementioned pressure disturbances have reflected off the axis, giving rise to a pressure plateau within the blast. Nowhere does the pressure exceed p_{ign}, so that the reaction has extinguished and partially consumed reactant is being convected downstream. At $t = 0.108$ the L-shock has weakened to the extent that it is no longer able to advance to the left in the lab frame and is being dragged downstream by the jetting solid. The pressure in the plateau within the blast now exceeds the pressures behind both shocks. The R-shock has traveled around the top of the cavity and has reached its nose. The secondary collapse of the cavity continues as its rear face is propelled towards the front face.

Stage II. Figure 15 displays the contour plots and the on-axis profiles of p and λ at four selected times. At $t = 0.112$ the decay of the blast continues unabated. The rear face of the cavity has just slammed into the front face, thereby generating a secondary blast region within which pressure is high enough to spawn an ignition kernel similar to that observed earlier for the spherical cavity. This region rapidly grows, both in size and strength, and at $t = 0.114$ it has reached and reflected off the axis, generating enormous pressures locally. In addition to the pressure peak, the on-axis plots now reveal the existence of the new site of reaction within the blast. At $t = 0.116$ the peak pressure at the axis has declined but remains significantly above the ignition threshold, and in fact, the consumption of reactant within the new blast is nearly complete. At $t = 0.118$ the new blast region has expanded further and is in the throes of vigorous reaction. At the top right edge of the blast one sees the by-now familiar hook, which is propagating the reaction-coupled shock, in effect a detonation, into the previously shocked but yet unreacted regions around the cavity.

Stage III. Contour plots and the on-axis profiles of p and λ at three selected times are shown in Figure 16 for this last stage. At $t = 0.122$ the hook identified at the end of Stage II continues its advancement, now

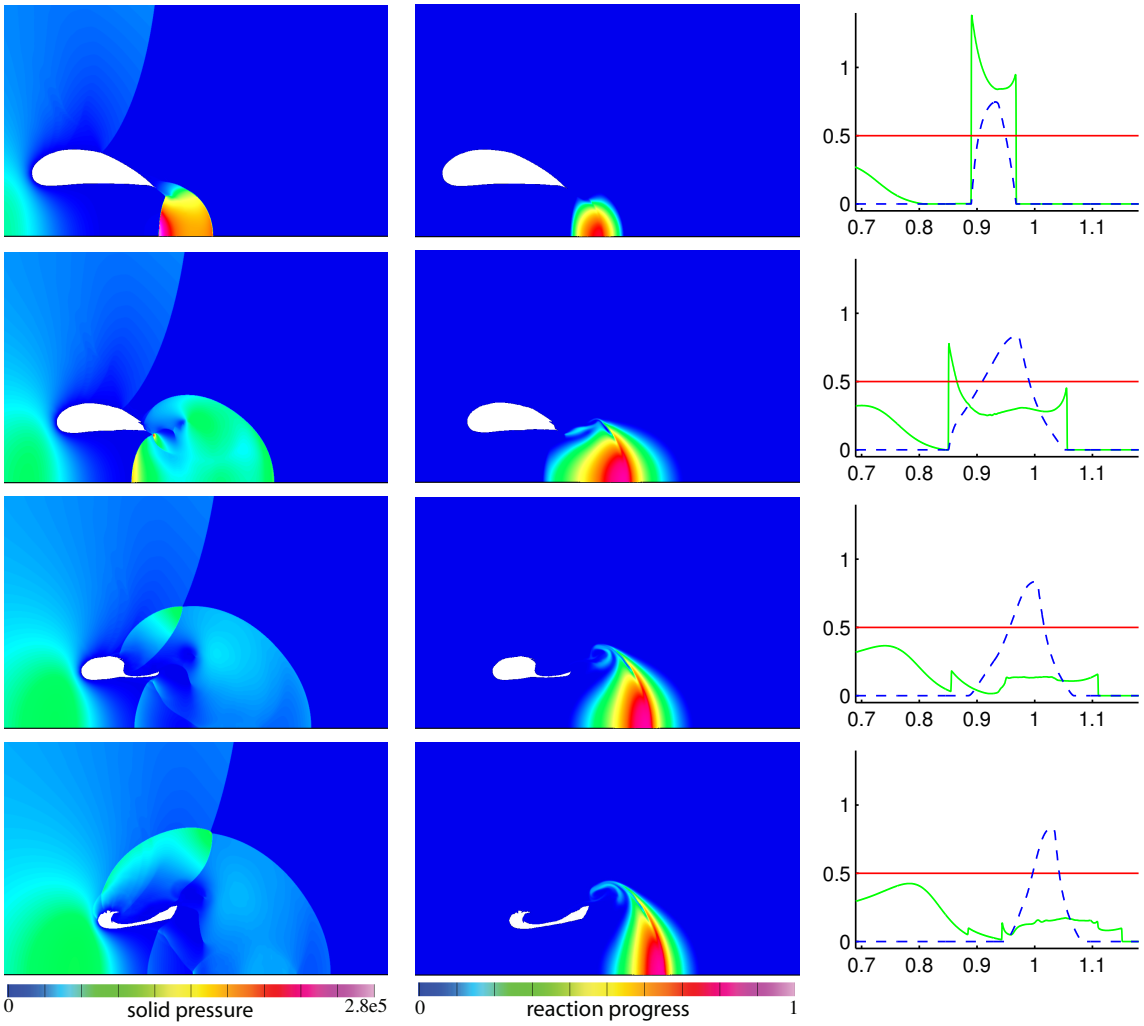

Figure 14: Long ellipsoidal cavity, $\sigma = 0.005$, Stage I. The panels show shaded contours of p (left), λ (middle) and on-axis profiles (right) at times $t = 0.092$, 0.098, 0.104 and 0.108. The on-axis plots show $p/2.0e5$ in green, λ in blue and $p_{\rm ign}/2.0e5$ in red.

into the partially reacted regions wherein the first blast had initiated a short-lived reaction. At $t = 0.128$ the downstream edge of the new blast is just behind the R-shock, and at $t = 0.130$ it has overtaken the R-shock. An expanding detonation is now fully established, and the reaction within it complete, except for a small region occupied by the remnants of the cavity. The upstream edge of the detonation is slightly stronger, as it propagates into previously shocked explosive.

4.2.2 Long cavity, $\sigma = 0.01$

For this larger reaction rate the evolution is faster and sufficiently distinct from the base case discussed above to merit a detailed description of its own, which we choose to present in two distinct stages.

Stage I. The contour plots and the on-axis profiles of p and λ at three selected times are displayed in Figure 17. At $t = 0.092$ the blast generated by the impact of the front face of the cavity on the rear face is strong, in that there is clear evidence, on axis and indeed throughout the blast, of reaction providing strong support strong to both the L- and the R-shocks. At $t = 0.096$ the blast has expanded and on axis both shocks are at near-equal strengths, with a zone of nearly complete reaction between them. If there

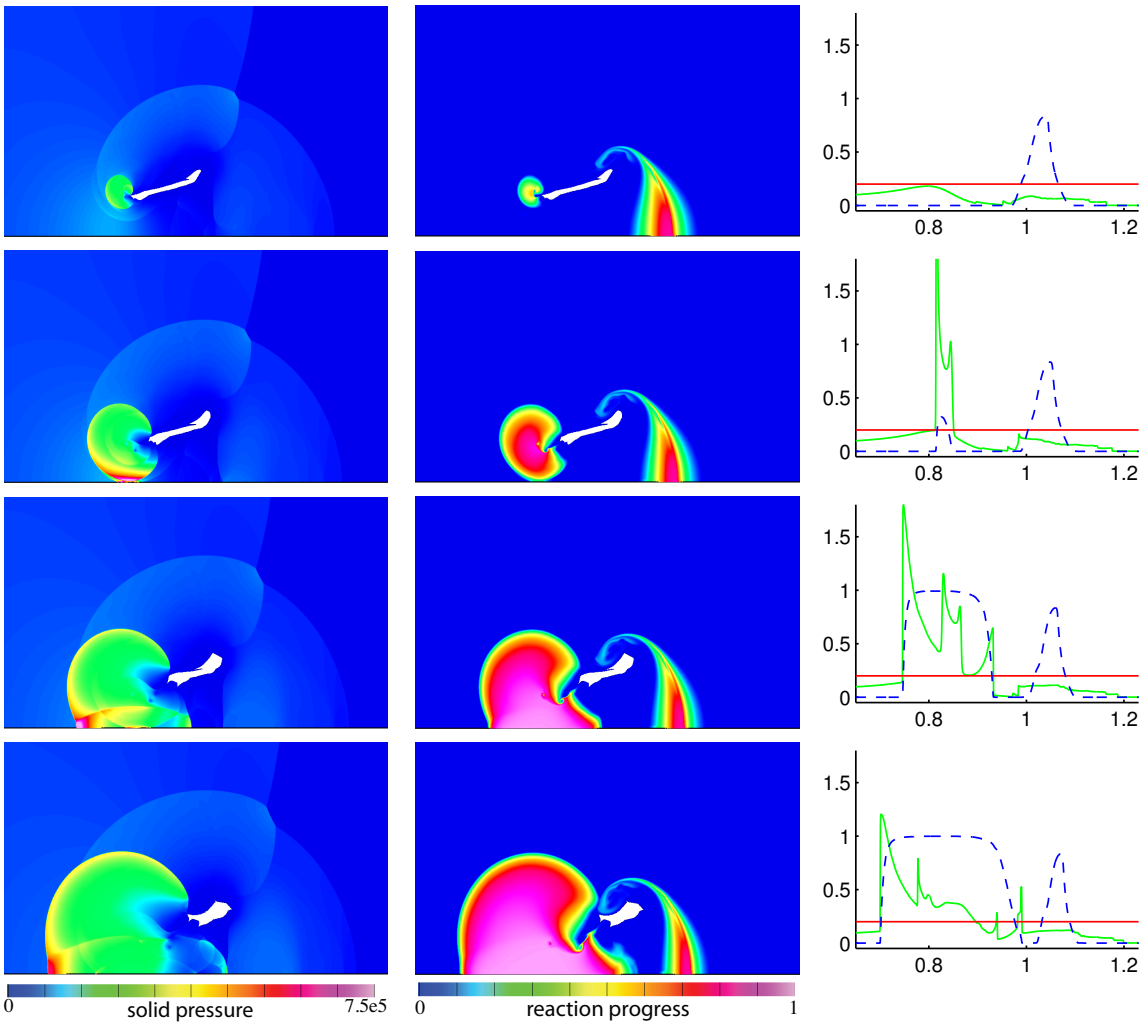

Figure 15: Long ellipsoidal cavity, $\sigma = 0.005$, Stage II. The panels show shaded contours of p (left), λ (middle) and on-axis profiles (right) at times $t = 0.112$, 0.114, 0.116 and 0.118. The on-axis plots show $p/5.0e5$ in green, λ in blue and $p_{\rm ign}/5.0e5$ in red.

is a weakness in the blast region, it is behind the upper end of the R-shock where it loses strength as it diffracts around the tail of the cavity, with a commensurately weaker reaction behind it. This state of affairs continues at $t = 0.098$, as the blast region expands. The R-shock has now developed a kink at its apex, separating the strongly reaction-supported segment on the right from the weaker arm on the left. Collision of the R-shock with the incident shock is imminent.

Stage II. The contour plots and the on-axis profiles of p and λ at three selected times are displayed in Figure 18. At $t = 0.102$ the R-shock has collided with the incident shock, thereby gaining strength and creating a high pressure pocket in which the hitherto weak reaction has intensified. This pocket of intense reaction grows in size and strengthens the R-shock, as seen in the $t = 0.104$ plots. The cavity undergoes a secondary collapse as before and, at $t = 0.106$, there is clear evidence of a collapse-induced secondary blast issuing from the nose of the cavity. This blast does not, however, play a major role as a new initiation site since both the L- and the R-shocks, fully supported by reaction behind them, have already evolved into detonations that are spreading and just about to fully surround the cavity.

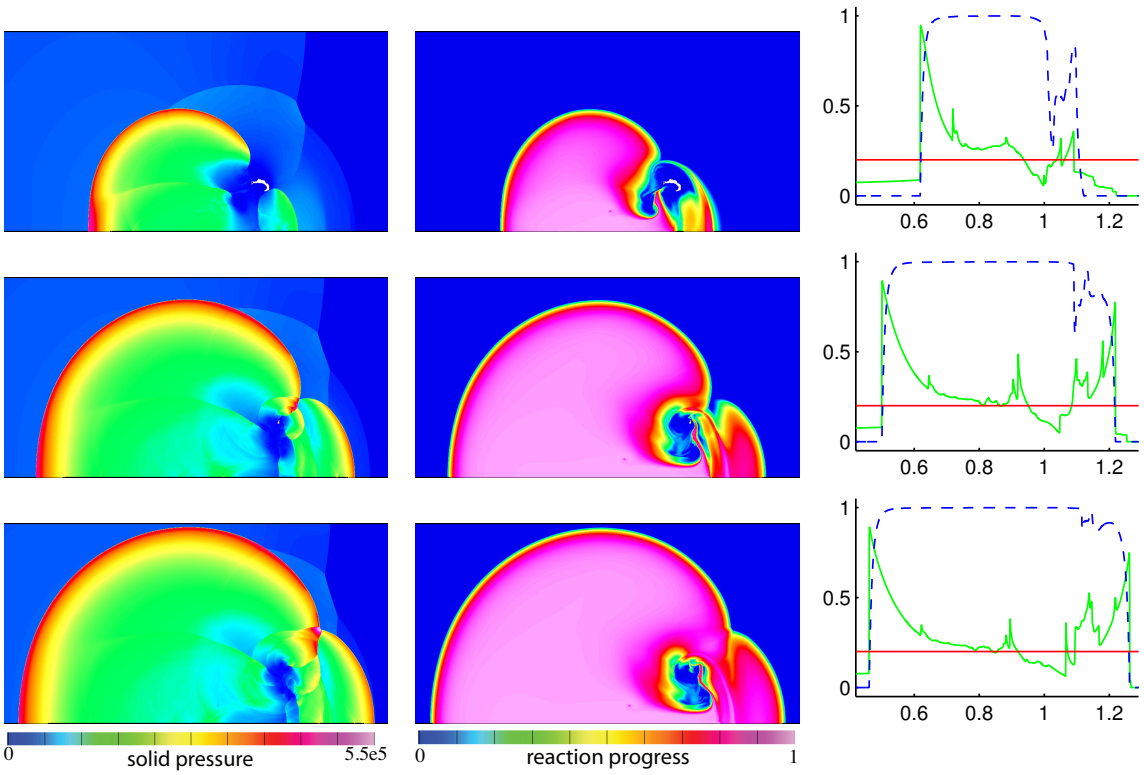

Figure 16: Long ellipsoidal cavity, $\sigma = 0.005$, Stage III. The panels show shaded contours of p (left), λ (middle) and on-axis profiles (right) at times $t = 0.122$, 0.128 and 0.130. The on-axis plots show $p/5.0e5$ in green, λ in blue and $p_{\rm ign}/5.0e5$ in red.

4.2.3 Long cavity, $\sigma = 0.001$

For this very weak reaction rate it is enough to present the results for four salient times, and this is done in the plots of Figure 19. At $t = 0.114$ the collapse-generated primary blast engulfs the cavity which has shrunk considerably in size. This blast is quite weak, and the highest pressure, caused by the secondary collapse, is found at the nose of the cavity. There are two sites of reaction; a narrow region within the blast where reaction had been initiated at an earlier time but is now extinct, having left behind a residue of partially reacted material, and a just-initiated weak reaction in the secondary blast. This latter region expands, and by $t = 0.122$ has collided with the axis to generate a pressure peak there and hence a more vigorous reaction. At $t = 0.130$ the expansion of the blast has caused the pressure peak to diminish, and the reaction has lost its vigor. At $t = 0.138$ the pressure nearly everywhere has fallen below the ignition threshold and reaction has completely shut down. The exception is a very narrow region on axis near the left boundary of the blast, where a weak reaction survives but is on its way to extinction.

4.3 The tall ellipsoidal cavity

We now examine shock interaction with an ellipsoidal cavity in the shape of an oblate spheroid. The major axis, now in the vertical direction, is twice as long as the minor axis, and the volume of the ellipsoid is the same as that of the spherical cavity. The incident shock retains the Mach number $M_s = 2.0$. Figure 20 shows the early behavior after the shock has interacted with the cavity, but before reaction begins. At the earliest time shown, $t = 0.028$, the incident shock has traveled nearly halfway across the cavity, and we observe the now familiar reflected expansion wave. The front face of the cavity has flattened as a result of the interaction, but an on-axis a solid jet has not formed. At later times we note the formation of a jet off-axis near the apex of the cavity. By the last time shown, $t = 0.052$, the incident shock is now diffracting

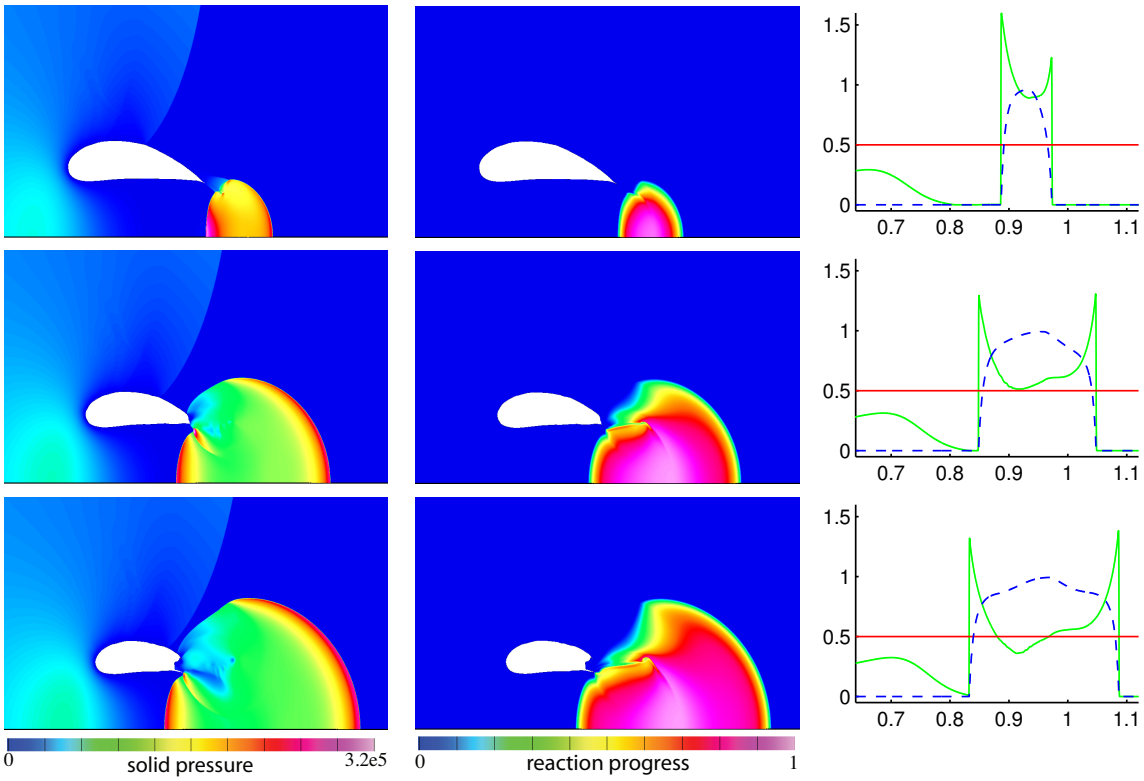

Figure 17: Long ellipsoidal cavity, $\sigma = 0.01$, Stage I. The panels show shaded contours of p (left), λ (middle) and on-axis profiles (right) at times $t = 0.092$, 0.096 and 0.098. The on-axis plots show $p/2.0e5$ in green, λ in blue and $p_{\text{ign}}/2.0e5$ in red.

around the rear face of the cavity, and the off-axis jet has nearly reached the rear face as well. The maximum pressure is below p_{ign} confirming that no reaction has occurred. Noting that the jet meets the rear face of the cavity off-axis, we have elected not to display the on-axis profiles of pressure and reaction progress as much of the activity is initiated and undergoes evolution off-axis.

4.3.1 Tall cavity, $\sigma = 0.005$

We consider two distinct stages of evolution for the base case.

Stage I. The contours of pressure and reaction progress at three selected times in the early stage are displayed in Figure 21. At $t = 0.058$ the front face of the cavity has collided with the rear face off-axis, thereby initiating the collapse by splitting the cavity into two lobes. The high-pressure blast region, bounded by the L- and the R-shocks, now appears between the lobes. The R-shock has already collided with the incident shock. However, nowhere has the pressure yet reached the ignition threshold. At $t = 0.060$ the pressure at the lower tip of the blast region has just risen above p_{ign} and the first hint of reaction there can be seen in the λ contour plot. At $t = 0.62$ the reaction at the bottom of the blast has intensified and the peak value of λ there has risen to 0.63. Coupling with the reaction has also caused a slight bulging in the profiles of the L- and R-shocks. The R-shock has progressed along the upper face of the upper lobe of the cavity, contributing to its shrinkage via a secondary collapse.

Stage II. The contours of pressure and reaction progress at three selected times in the late stage are displayed in Figure 22. At $t = 0.066$ the secondary collapse of the upper lobe of the cavity is nearly complete, but the resulting blast is too weak to be of significance as regards initiation. At the same time the bottom of the primary blast has collided with the axis, generating reflected shocks and a local pressure at 1.16e6 units, more than ten times the ignition threshold. Intense reaction ensues and couples strongly with both

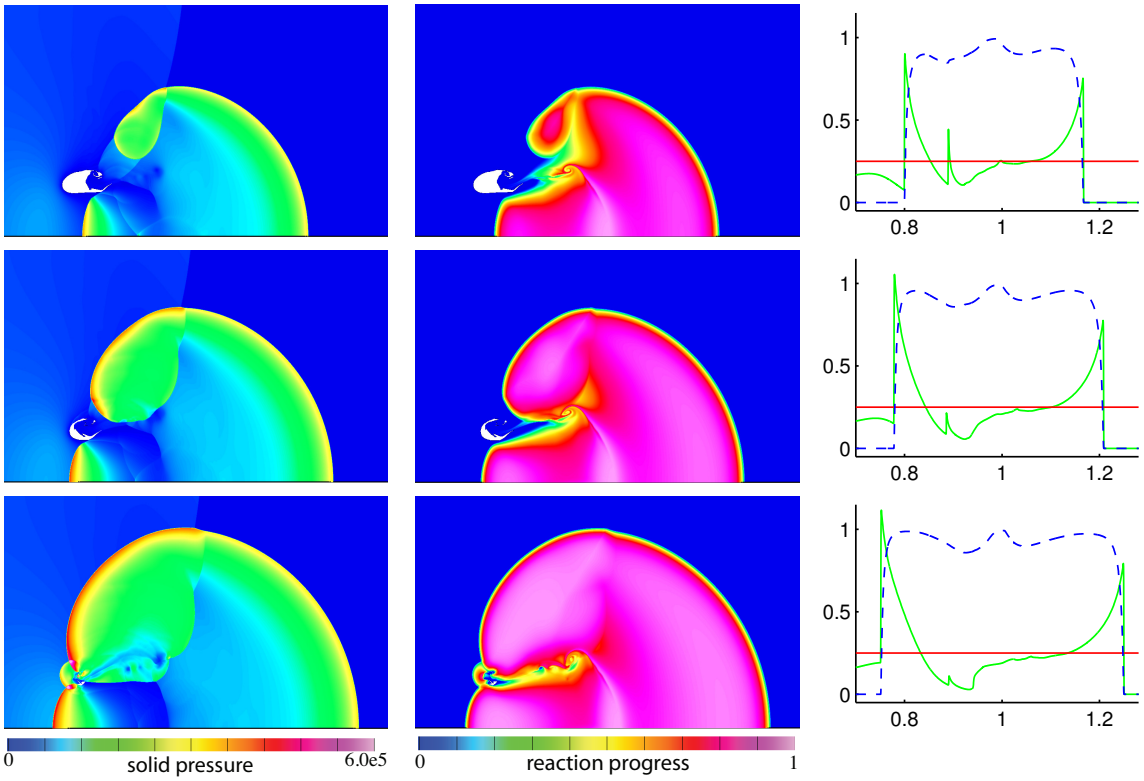

Figure 18: Long ellipsoidal cavity, $\sigma = 0.01$, Stage II. The panels show shaded contours of p (left), λ (middle) and on-axis profiles (right) at times $t = 0.102$, 0.104 and 0.106. The on-axis plots show $p/4.0e5$ in green, λ in blue and $p_{\rm ign}/4.0e5$ in red.

the bounding shocks. At $t = 0.068$ the blast region expands and the maximum pressure is relieved to the level of 6.0e5 units. The reflected shocks travel upwards, raising the pressure broadly and causing reaction completion in an expanding domain. At $t = 0.072$ the nearly full strength detonation has been established.

4.3.2 Tall cavity, $\sigma = 0.01$

At this high reaction rate, all the events occurring at the slower rate still persist, but the evolution is faster. The contours of pressure and reaction progress at four selected times are displayed in Figure 23. At $t = 0.062$ the collapse has been initiated, the blast region has formed, and the pressure within the blast region has risen sufficiently to generate significant reaction there. At $t = 0.066$ the bottom of the blast has collided with the axis, generating reflected shocks and a high local pressure. The contour plot of λ indicates nearly full reactant consumption throughout the blast and the formation of a detonation. At $t = 0.068$ the reflected shocks are moving away from the axis into the fully reacted region, and the detonation is expanding. At $t = 0.072$ the fully-established detonation continues to propagate outwards.

4.3.3 Tall cavity, $\sigma = 0.001$

We now consider a very weak reaction rate to explore whether it is possible for a detonation to form. The relevant contour plots of p and λ are displayed in Figure 24 at four selected times. At $t = 0.060$ the collapse has been initiated, the blast region has formed, and a mere hint of reaction can be found at the bottom of the blast. At $t = 0.066$ the blast has impacted the axis, and although a high pressure has developed behind the reflected shock, the resulting reaction is still weak. At $t = 0.072$ the L-shock has been strengthened due to support by the reaction, but the coupling continues to remain weak. At $t = 0.076$ the blast has expanded with little additional strengthening of the L-shock. Nowhere has the reaction reached

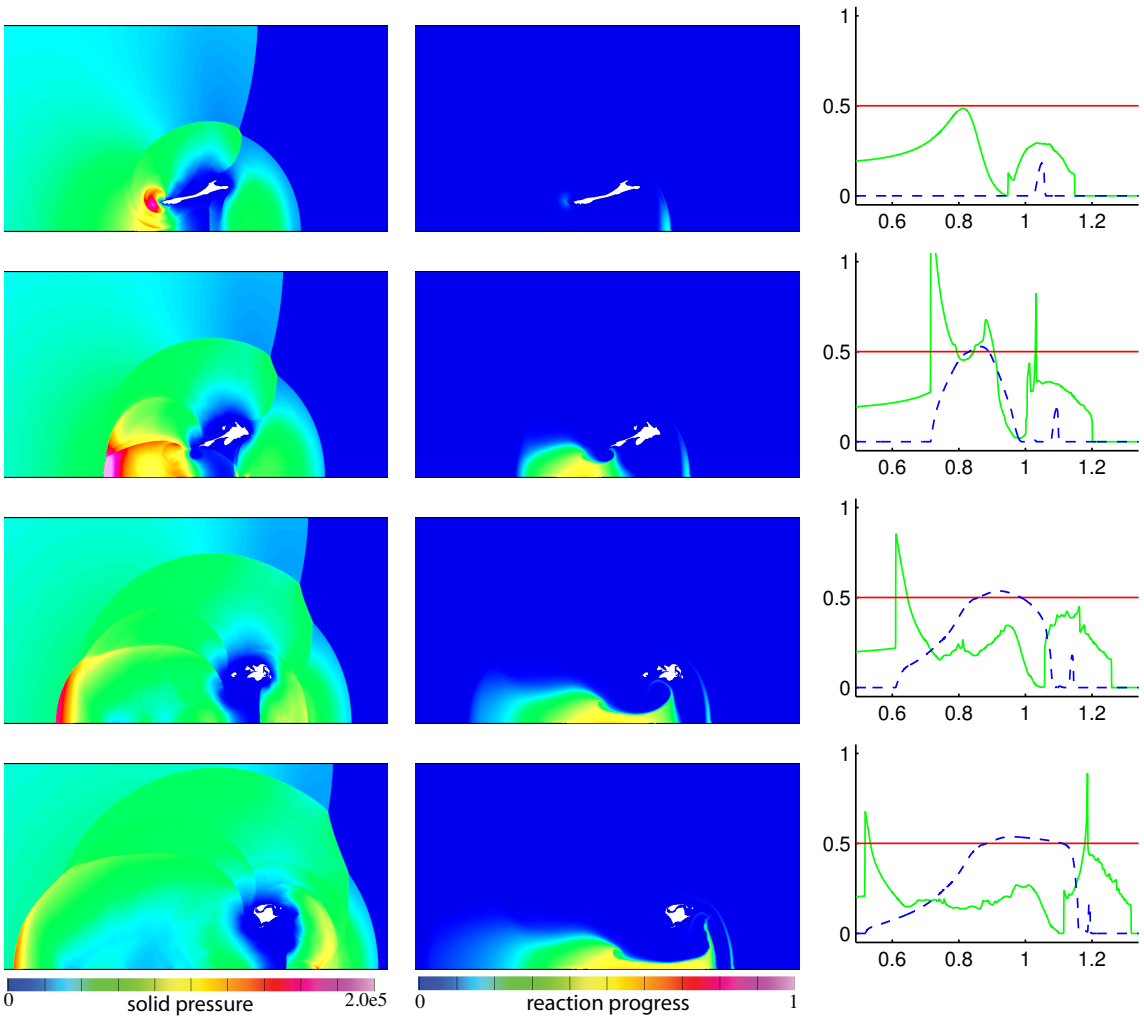

Figure 19: Long ellipsoidal cavity, $\sigma = 0.001$. The panels show shaded contours of p (left), λ (middle) and on-axis profiles (right) at times $t = 0.114$, 0.122, 0.130 and 0.138. The on-axis plots show $p/2.0e5$ in green, λ in blue and $p_{\rm ign}/2.0e5$ in red.

completion. The extent of shock-reaction coupling is expected to continue to diminish with time.

5 Conclusions

In this paper we have examined, computationally, the collapse of a gas-filled cavity brought about by its interaction with a planar shock propagating through the solid explosive in which the cavity is embedded. The aim has been to explore the role of cavity collapse as a means of reaction initiation. Results have been obtained for an incident shock of a given strength. Three different cavity shapes have been investigated: sphere, prolate spheroid (long) and oblate spheroid (tall). Each shape has been studied for a range of values of the prefactor σ in the pressure-dependent reaction rate, which upon our choice of scaling can be interpreted as a measure of either the size of the cavity for a given reaction rate or the strength of the reaction rate for a given cavity size.

For the spherical cavity and at the base value of $\sigma = 0.005$, it has been found that the impact of the shock causes the front face of the cavity to fold inwards and collide with the rear face, thereby initiating the collapse of the cavity and producing an expanding region of high pressure (the blast region) enclosed within

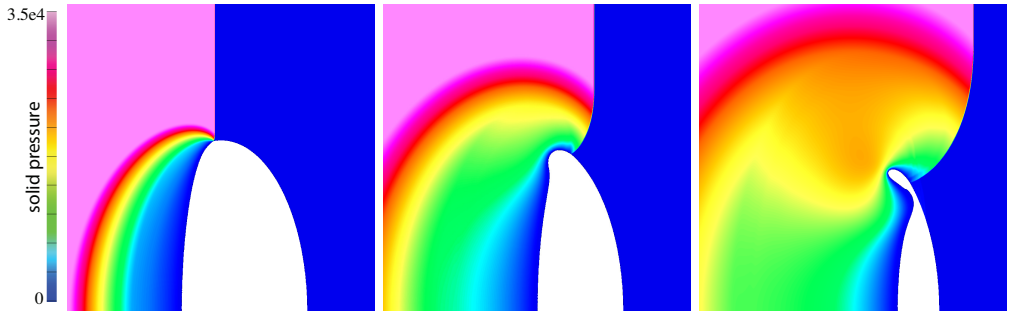

Figure 20: Tall ellipsoidal cavity: shaded contours of pressure p at times $t = 0.028,\ 0.040$ and 0.052 (left to right). Reaction has not yet begun, and collision between the off-axis solid jet and rear face of the cavity is imminent at $t = 0.052$.

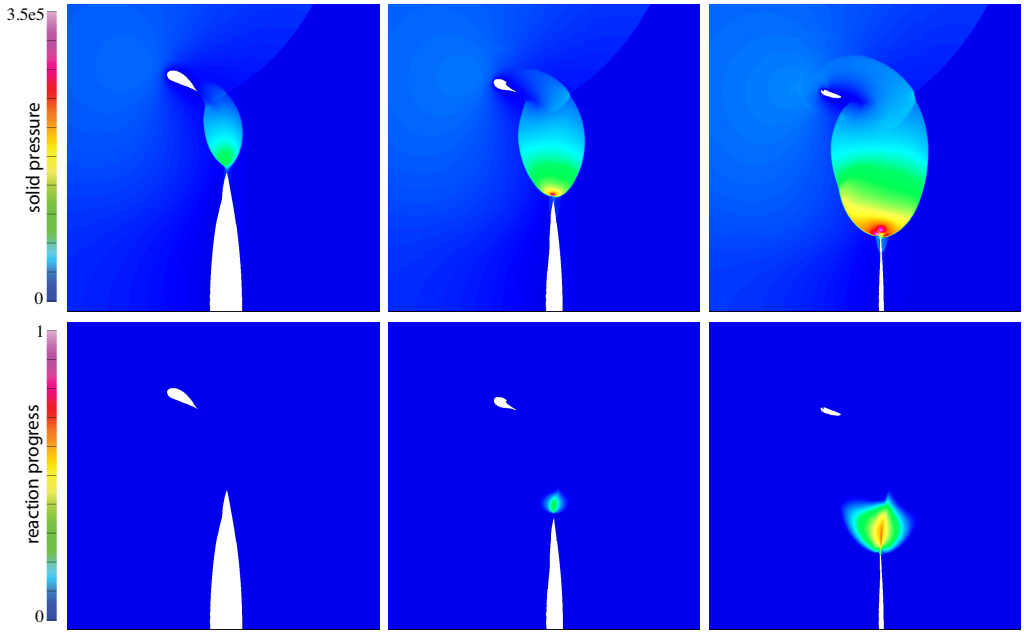

Figure 21: Tall ellipsoidal cavity, $\sigma = 0.005$, Stage I. The panels show shaded contours of p (top) and λ (bottom) at times $t = 0.058$, 0.060 and 0.062 (left to right).

two shocks, one propagating upstream (L-shock) into the solid already compressed by the incident shock and the other advancing downstream (R-shock) into the yet unprocessed solid. Within this region the pressure rises to a level high enough to initiate reaction, which couples preferentially with the L-shock, strengthens it, and leads to the formation of a curved detonation. The R-shock, weakened due to insufficient support from reaction, propagates around the top face of the by-now shrunk cavity, thereby collapsing it further and leading to a secondary blast region near the nose of the cavity. High pressure in this blast region leads to significant reaction there, which couples to the curved detonation already formed behind the L-shock and ultimately results in a nearly spherical detonation propagating outwards.

Halving the value of σ for the spherical cavity produces a similar outcome eventually, but the evolutionary details are somewhat different. The blast region enclosed by the L- and R-shocks is weaker, as is the coupling of the reaction with the L-shock. Unlike the base case, a detonation no longer forms behind the L-shock. Nevertheless, the propagation of the L- and R-shocks around the shrunk cavity still causes it to collapse further, leading to a secondary blast region off-axis as in the base case. The resulting reaction within this secondary blast region is found to be sufficient to generate a detonation spreading outwards. Reflection at the axis of symmetry strengthens the detonation, and in due course, a nearly spherical detonation is

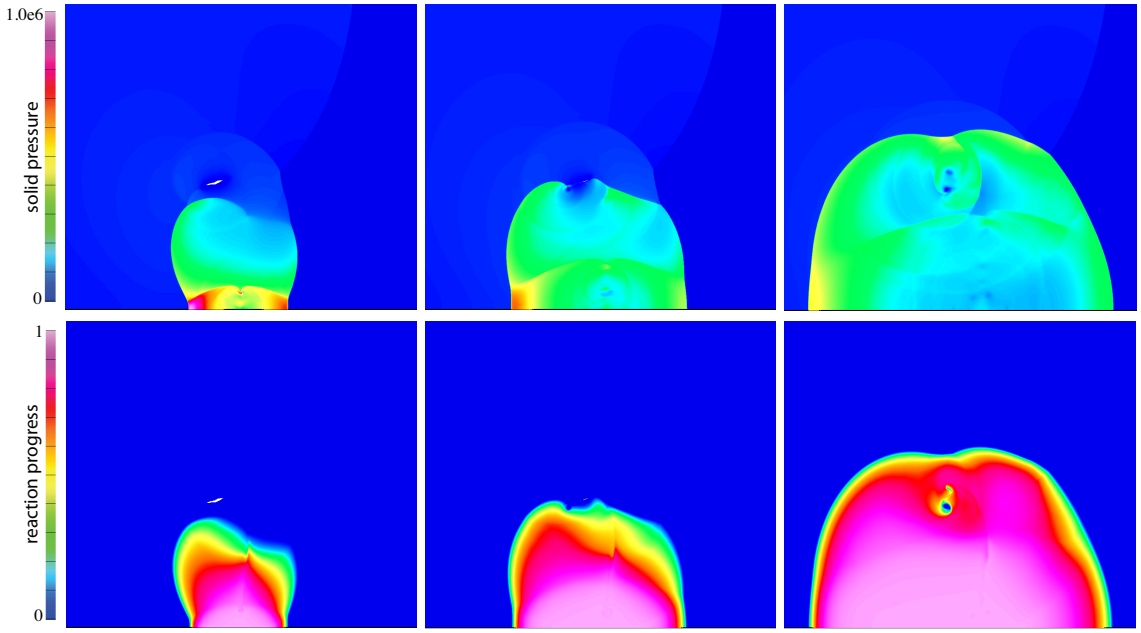

Figure 22: Tall ellipsoidal cavity, $\sigma = 0.005$, Stage II. The panels show shaded contours of p (top) and λ (bottom) at times $t = 0.066$, 0.068 and 0.072 (left to right).

produced as before. Reducing σ by a factor of 10 from the base value causes only a temporary and weak coupling of reaction with pressure, and after a partial consumption of reactant the reaction extinguishes everywhere. Increasing the value of σ to twice the base value produces a very strong post-collapse blast, in which reaction couples with both the L- and the R-shocks, and a spherical detonation is swiftly generated.

For the long cavity and at the base value of $\sigma = 0.005$, the post-collapse shocks are strong enough to initiate reaction nearly everywhere within the blast region. Although a significant amount of reactant consumption occurs there, the reaction is unable to couple robustly with the shocks which, as a result, weaken swiftly, thereby extinguishing the reaction. As in the base case of the spherical cavity, the propagation of the L- and R-shocks around the remnants of the long cavity causes a secondary collapse. High pressure within the resulting blast spawns a new ignition kernel off-axis. Reflection of the expanding blast from the axis of symmetry raises the pressure further still, creating an expanding region of high pressure at the axis, at the upstream boundary of which a detonation is formed. As this detonation curves and hooks around,

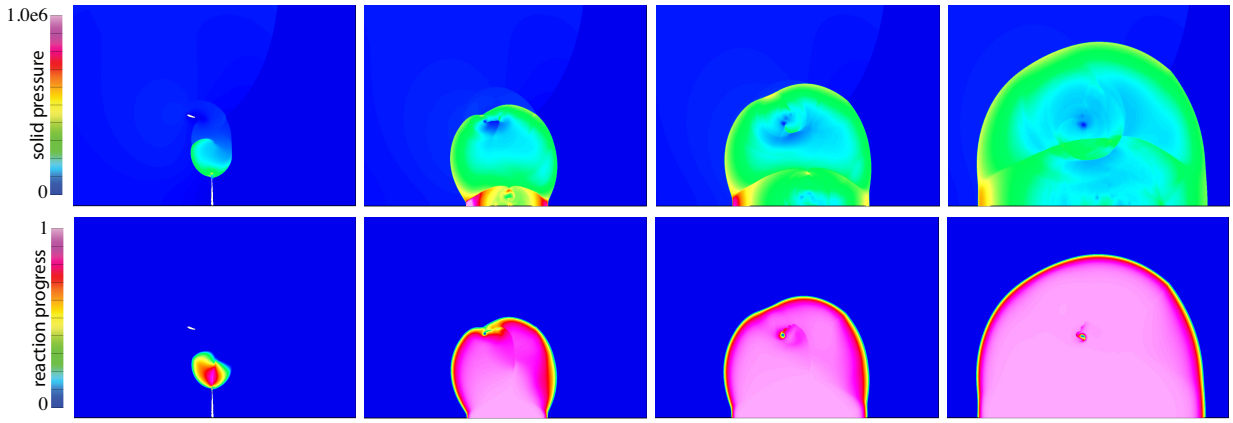

Figure 23: Tall ellipsoidal cavity, $\sigma = 0.01$. The panels show shaded contours of p (top) and λ (bottom) at times $t = 0.062$, 0.066, 0.068 and 0.072 (left to right).

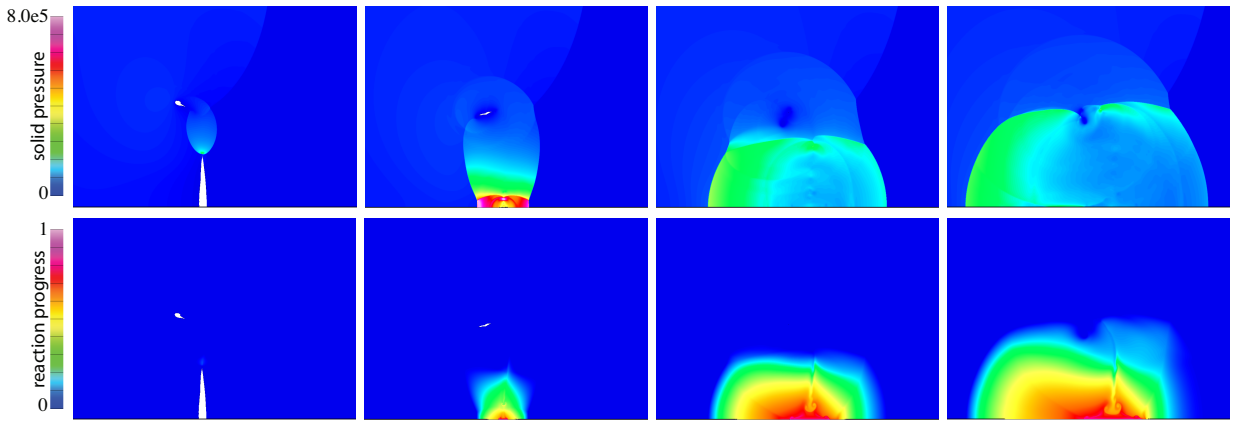

Figure 24: Tall ellipsoidal cavity, $\sigma = 0.001$. The panels show shaded contours of p (top) and λ (bottom) at times $t = 0.060$, 0.066, 0.072 and 0.076 (left to right).

a second detonation branch forms at the right extremity of the high-pressure region. The two branches eventually merge into a spherical detonation. Reducing σ by a factor of 10 from the base value results in only a partial reactant consumption followed by reaction extinction. Increasing the value of σ to twice the base value produces, not unexpectedly, a strong post-collapse blast with attendant reaction coupling and detonation formation. Unlike the spherical geometry, it is the detonation associated with the R-shock that hooks around the collapsed cavity to merge with the detonation traveling upstream to form the spherical detonation.

For the tall cavity and at the base value of $\sigma = 0.005$, the situation is different in that the collision between the front and rear faces of the cavity occurs off-axis. The resulting blast travels radially towards the axis where its reflection generates intense pressures, higher than those seen for either of the other shapes discussed above. A fully matured detonation is established rapidly. Doubling σ accelerates the processes observed for the base case, while reducing σ by a factor of 10 causes the weak initial reaction to fizzle out.

It is useful to recall the relationship between σ and the cavity size. The characteristic dimension of each cavity, the diameter of a sphere of the same volume as the cavity, has been chosen to be $d = 0.4 \times x_{\rm ref}$. The relation (8) between the reference length $x_{\rm ref}$ and the CJ reaction-zone length $x_{\rm rz}$ then leads to the relation $d = 2000 \times \sigma$. Thus the four values $\sigma = 0.001$, 0.0025, 0.005 and 0.01 employed in this study correspond, respectively to d being twice, five times, ten times, and twenty times the reaction-zone thickness, respectively.

We draw several conclusions from the results. First, a cavity that is only twice the size of the reaction-zone thickness is unable to amplify the post-incident-shock pressure to a level high enough to produce sustained reaction, independent of its shape. Second, a cavity of size five times the reaction-zone thickness or larger provides ample pressure amplification to lead to a detonation, again independent of shape. Third, for a given volume, the tall cavity is the most efficient in the generation of high-pressure hot spots and the subsequent evolution to detonation. Finally, the sites of ignition and the path to detonation are not only shape-dependent, but can also vary with cavity size even for the same shape. Earlier studies had suggested that the primary blast at the rear of the cavity is the site of ignition. Our results have shown that such is not always the case, and that off-axis ignition sites have important roles to play, even for a spherical cavity.

Some limitations of this study must be pointed out. First, the results have been confined to a single cavity. The more practical situation of a group of cavities placed sufficiently close to one another is liable to behave synergistically, in that the pressure field generated by the lead cavity could well present a stronger incident disturbance to neighboring cavities than that experienced by the lead cavity. A weaker stimulus may therefore provoke a detonation in this case. Second, the quantitative conclusions drawn from our results depend strongly on the equations of state chosen and the reaction rate adopted. Third, the pressure-dependent reaction rate and the absence of diffusion restricts the competing mechanisms responsible for initiation strictly to gasdynamic phenomena. Thus, regions of high pressure are created via shock focusing, shock reflection, and shock-shock interaction, while loss of pressure takes place via diffraction and expansion. A

temperature-dependent reaction rate would require reinstatement of diffusion as a significant loss mechanism. Despite these limitations, however, the present study has revealed new ignition processes in heterogeneous explosives that should inform subsequent studies.

6 Appendix

We consider the structure of a planar, Chapman-Jouguet detonation in the solid. Assuming that the detonation is propagating at speed D into a stationary state characterized by the suffix 1, conservation of mass, momentum and energy provide the conditions

$$\rho(D-u) = \rho_1 D, \tag{12}$$

$$p+\rho(D-u)^2 = p_1+\rho_1 D^2, \tag{13}$$

$$h+\frac{1}{2}(D-u)^2 = h_1+\frac{1}{2}D^2. \tag{14}$$

Here, h is the enthalpy given by

$$h = e+\frac{p}{\rho} = \frac{(1+w_1)p+w_2}{\rho} - \lambda q_s, \tag{15}$$

for the equation of state in (5) with $q = q_s$ for the solid. We note that

$$h_1 = \frac{\big(1+w_1^{(u)}\big)p_1+w_2^{(u)}}{\rho_1}, \tag{16}$$

since $\lambda = 0$ and $\mathbf{w} = \mathbf{w^{(u)}}$ at state 1. Now, (15) and (16) yield

$$h-h_1 = \frac{(1+w_1)p+w_2}{\rho} - \frac{\big(1+w_1^{(u)}\big)p_1+w_2^{(u)}}{\rho_1} - \lambda q_s. \tag{17}$$

Elimination of u from (12) and (13) provides the Rayleigh line

$$p-p_1 = J^2\left(\frac{1}{\rho_1}-\frac{1}{\rho}\right), \tag{18}$$

where $J = \rho_1 D$ is the mass flux through the steady detonation wave. Elimination of u between (12) and (14) leads to

$$h-h_1 = \frac{1}{2}J^2\left(\frac{1}{\rho_1^2}-\frac{1}{\rho^2}\right),$$

and then, the use of (18) to eliminate J yields

$$h-h_1 = \frac{1}{2}(p-p_1)\left(\frac{1}{\rho_1}+\frac{1}{\rho}\right). \tag{19}$$

By virtue of (17), equation (19) transforms into

$$\frac{1}{2}(p-p_1)\left(\frac{1}{\rho_1}+\frac{1}{\rho}\right) = \frac{(1+w_1)p+w_2}{\rho} - \frac{\big(1+w_1^{(u)}\big)p_1+w_2^{(u)}}{\rho_1} - \lambda q_s, \tag{20}$$

which specifies a family of Hugoniot curves, parameterized by λ. To find the intersection of the Rayleigh line and a Hugoniot curve for any choice of λ, we eliminate ρ between (18) and (20) to get

$$\frac{1}{2}(p-p_1)\left(\frac{2}{\rho_1}-\frac{p-p_1}{J^2}\right) = \big[(1+w_1)p+w_2\big]\left(\frac{1}{\rho_1}-\frac{p-p_1}{J^2}\right) - \frac{\big(1+w_1^{(u)}\big)p_1+w_2^{(u)}}{\rho_1} - \lambda q_s. \tag{21}$$

On setting $P = p - p_1$, (21) can be rearranged into the quadratic

$$P^2 - \frac{2\rho_1 w_1}{2w_1+1}\left[D^2 - \frac{(1+w_1)p_1 + w_2}{\rho_1 w_1}\right]P + \frac{2D^2\rho_1^2}{2w_1+1}\left[\lambda q_s - \frac{\big(w_1 - w_1^{(u)}\big)p_1 + \big(w_2 - w_2^{(u)}\big)}{\rho_1}\right] = 0. \qquad (22)$$

Here we have replaced J in favor of $D = J/\rho_1$. For a specified D the appropriate solution of this quadratic yields the pressure increment $P = p - p_1$ as a function of λ. With P known, the original conservation conditions determine the other state variables, ρ and u.

6.1 The CJ state

At the CJ point the two roots of the quadratic in (22) are equal when λ is set to 1. We note that $\mathbf{w} = \mathbf{w}^{(r)}$ at $\lambda = 1$. Therefore equation (22) reduces to

$$P^2 - \frac{2\rho_1 w_1^{(r)}}{2w_1^{(r)}+1}\left[D^2 - \frac{\big(1+w_1^{(r)}\big)p_1 + w_2^{(r)}}{\rho_1 w_1^{(r)}}\right]P + \frac{2D^2\rho_1^2}{2w_1^{(r)}+1}\left[q_s - \frac{\big(w_1^{(r)} - w_1^{(u)}\big)p_1 + \big(w_2^{(r)} - w_2^{(u)}\big)}{\rho_1}\right] = 0. \qquad (23)$$

The equal-roots condition

$$\left[D^2 - \frac{\big(1+w_1^{(r)}\big)p_1 + w_2^{(r)}}{\rho_1 w_1^{(r)}}\right]^2 = \frac{2(2w_1^{(r)}+1)}{\big(w_1^{(r)}\big)^2}D^2\left[q_s - \frac{\big(w_1^{(r)} - w_1^{(u)}\big)p_1 + \big(w_2^{(r)} - w_2^{(u)}\big)}{\rho_1}\right] \qquad (24)$$

determines the CJ speed $D_{\rm CJ}$. We define

$$\begin{aligned}\alpha &= \frac{\big(1+w_1^{(r)}\big)p_1 + w_2^{(r)}}{\rho_1 w_1^{(r)}},\\ \beta &= \frac{2w_1^{(r)}+1}{\big(w_1^{(r)}\big)^2}\left[q_s - \frac{\big(w_1^{(r)} - w_1^{(u)}\big)p_1 + \big(w_2^{(r)} - w_2^{(u)}\big)}{\rho_1}\right],\end{aligned}$$

so that (24) condenses into

$$(D^2 - \alpha)^2 = 2\beta D^2,$$

and yields the root $D_{\rm CJ}$ as

$$D_{\rm CJ}^2 = (\alpha+\beta) + \sqrt{(\alpha+\beta)^2 - \alpha^2}. \qquad (25)$$

Once $D_{\rm CJ}$ is known, (23) determines $P_{\rm CJ}$ to be

$$P_{\rm CJ} = \frac{\rho_1 w_1^{(r)}}{2w_1^{(r)}+1}\left[D_{\rm CJ}^2 - \frac{\big(1+w_1^{(r)}\big)p_1 + w_2^{(r)}}{\rho_1 w_1^{(r)}}\right].$$

Then,

$$p_{\rm CJ} = p_1 + P_{\rm CJ}, \qquad \frac{1}{\rho_{\rm CJ}} = \frac{1}{\rho_1} - \frac{P_{\rm CJ}}{\rho_1^2 D_{\rm CJ}^2}, \qquad u_{\rm CJ} = D_{\rm CJ}\left(1 - \frac{\rho_1}{\rho_{\rm CJ}}\right),$$

and the CJ state is completely determined.

We are interested, in particular, at the CJ detonation propagating in the region $\tilde{\Omega}_s$ behind the incident shock; see Figure 1. The density and pressure in that region are given in Table 1. The von-Neumann and CJ states associated with the detonation are listed in Table 2.

6.2 Reaction-wave structure

The structure of the reaction zone for wave speed $D_{\rm CJ}$ is determined by the traveling-wave version of the rate law,

$$(D_{\rm CJ} - u)\lambda_x = -\mathcal{R}, \qquad (26)$$

States	von-Neumann	CJ
D		22.67
p	4.9025e5	4.5941e5
ρ	4.3110e3	4.1952e3

Table 2: Steady detonation states.

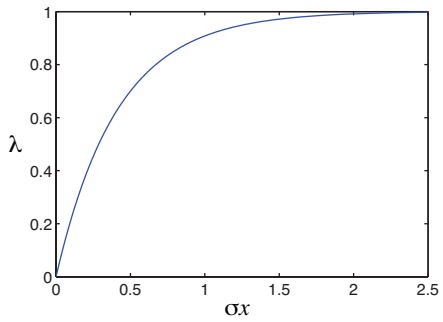

Figure 25: Reaction-zone structure, as determined by the profile of λ against σx.

where $\mathcal{R}$ is the pressure-dependent reaction rate defined in (4). We shall assume that the pressure at the end of the reaction zone exceeds the pressure threshold $p_{\rm ign}$ so that the reaction is not extinguished prior to complete consumption of the reactant. Integration of (26) requires p and u to be known functions of λ. The expression for $p(\lambda)$ comes from solving the quadratic (22) with $D = D_{\rm CJ}$, which can be expressed concisely as

$$P^2 - 2bP + c = 0,$$

where

$$b(\lambda) = \frac{\rho_1 w_1}{2w_1 + 1}\left[D_{\rm CJ}^2 - \frac{(1+w_1)p_1 + w_2}{\rho_1 w_1}\right],$$

$$c(\lambda) = \frac{2\rho_1^2 (D_{\rm CJ})^2}{2w_1 + 1}\left[\lambda q_s - \frac{\left(w_1 - w_1^{(u)}\right)p_1 + \left(w_2 - w_2^{(u)}\right)}{\rho_1}\right].$$

In these equations, $\mathbf{w} = (\mathbf{1} - \lambda)\mathbf{w^{(u)}} + \lambda \mathbf{w^{(r)}}$. Based on the results for an ideal gas, one expects $b(\lambda)$ to be positive and $c(\lambda)$ to be monotonically increasing from zero as λ increases through the reaction zone from zero to unity. The quadratic for P has the roots

$$P = b(\lambda) \pm \sqrt{b^2(\lambda) - c(\lambda)}.$$

We choose the plus sign, which corresponds to a shock at the head of the reaction zone and a decreasing pressure through the reaction zone. With P known, $p = p_1 + P$ yields the pressure p and then, u is given by

$$u = \frac{P}{\rho_1 D_{\rm CJ}}.$$

One is now in a position to integrate (26) for $\lambda(x)$. The resulting structure appears in Figure 25, as the graph of λ against the scaled spatial coordinate σx. We note, from the figure, that the dimensionless reaction-zone length $x_{\rm rz}$ is given by

$$\sigma x_{\rm rz} = 2 \times 10^{-4}, \tag{27}$$

where we have assigned the end of the reaction zone to correspond to $\lambda = 0.99$.

References

[1] M. Ozlem, D. W. Schwendeman, A. K. Kapila, W. D. Henshaw, A numerical study of shock-induced cavity collapse, Shock Waves 22 (2012) 89–117.

[2] N. K. Bourne, On the collapse of cavities, Shock Waves 11 (2002) 447–455.

[3] N. K. Bourne, J. E. Field, Explosive ignition by the collapse of cavities, Proc. R. Soc. Lond. A 455 (1999) 2411–2426.

[4] A. B. Swantek, J. M. Austin, Collapse of void arrays under stress wave loading, J. Fluid Mech. 649 (2010) 399–427.

[5] A. Milne, N. Bourne, Experimental and numerical study of temperature in cavity collapse, in: N. T. M.D. Furnish, Y. Horie (Eds.), Shock Compression of Condensed Matter, Vol. CP620, American Institute of Physics, 2002, pp. 131–176.

[6] L. B. Tran, H. S. Udaykumar, Simulations of void collapse in an energetic material, part i: inert case, J. Propuls. Power 22 (2006) 947–958.

[7] L. B. Tran, H. S. Udaykumar, Simulations of void collapse in an energetic material, part ii: reactive case, J. Propuls. Power 22 (2006) 959–974.

[8] A. Kapahi, H. S. Udaykumar, Dynamics of void collapse in shocked energetic materials: physics of void-void interaction, Shock Waves 23 (2013) 537–558.

[9] E. Lauer, X. Y. Hu, S. Hickel, N. A. Adams, Numerical investigation of collapsing cavities, Phys. Fluids 24 (5) (2012) 052104–1–052104–24.

[10] L. Michael, N. Nikiforakis, The temperature field around collapsing cavities in condensed-phase explosives, in: The Fifteenth Symposium (International) on Detonation, 2014.

[11] R. Abgrall, How to prevent pressure oscillations in mulicomponent flow calculations: A quasi conservative approach, J. Comput. Phys. 125 (1996) 150–160.

[12] R. Saurel, R. Abgrall, A simple method for compressible multifluid flows, SIAM J. Sci. Comput. 21 (3) (1999) 1115–1145.

[13] D. W. Schwendeman, C. W. Wahle, A. K. Kapila, The Riemann problem and a high-resolution Godunov method for a model of compressible two-phase flow, J. Comput. Phys. 212 (2006) 490–526.

[14] W. D. Henshaw, D. W. Schwendeman, An adaptive numerical scheme for high-speed reactive flow on overlapping grids, J. Comput. Phys. 191 (2) (2003) 420–447.

[15] A. K. Kapila, D. W. Schwendeman, J. B. Bdzil, W. D. Henshaw, A study of detonation diffraction in the ignition-and-growth model, Combust. Theory and Modeling 11 (2007) 781–822.

[16] D. W. Schwendeman, C. W. Wahle, A. K. Kapila, A study of detonation evolution and structure for a model of compressible two-phase reactive flow, Combust. Theory and Modeling 12 (2008) 159–204.

[17] J. B. Banks, D. W. Schwendeman, A. K. Kapila, W. D. Henshaw, A study of detonation propagation and diffraction with compliant confinement, Combust. Theory Modeling 12 (2008) 769–808.

[18] W. D. Henshaw, Overture: An Object-Oriented Toolkit for Solving Partial Differential Equations in Complex Geometries, `http://www.overtureframework.org/`, [Online; accessed 8/1/2014].

[19] D. W. Schwendeman, A. K. Kapila, W. D. Henshaw, A study of detonation diffraction and failure for a model of compressible two-phase reactive flow, Combust. Theory and Modeling 14 (2010) 331–266.

[20] E. F. Toro, Riemann Solvers and Numerical Methods for Fluid Dynamics, Springer, Berlin, 1999.

[21] W. D. Henshaw, D. W. Schwendeman, Parallel computation of three-dimensional flows using overlapping grids with adaptive mesh refinement, J. Comput. Phys. 227 (2008) 7469–7502.

[22] D. W. Schwendeman, A. K. Kapila, W. D. Henshaw, A hybrid multiphase mixture model of detonation diffraction with compliant confinement, Comptes Rendus Mecanique 340 (2012) 804–817.